석 사 학 위 논 문

Master's Thesis

수중 폭발을 고려한 부유식 구조물의 유탄성 해석

Hydroelastic analysis of floating structures subjected to underwater explosive bubbles

2019

최 형 규（崔 亨 圭 Choi, Hyunggyu）

한 국 과 학 기 술 원

Korea Advanced Institute of Science and Technology

석 사 학 위 논 문

수중 폭발을 고려한
부유식 구조물의 유탄성 해석

2019

최 형 규

한 국 과 학 기 술 원

기계항공공학부/기계공학과

수중 폭발을 고려한
부유식 구조물의 유탄성 해석

최 형 규

위 논문은 한국과학기술원 석사학위논문으로
학위논문 심사위원회의 심사를 통과하였음

2018년 12월 17일

심사위원장 이 필 승 (인)

심 사 위 원 김 대 겸 (인)

심 사 위 원 이 강 헌 (인)

Hydroelastic analysis of floating structures subjected to underwater explosive bubbles

Choi, Hyunggyu

Advisor: Lee, Phill-Seung

A thesis submitted to the faculty of
Korea Advanced Institute of Science and Technology in
partial fulfillment of the requirements for the degree of
Master of Science in Mechanical Engineering

Daejeon, Korea
December 17, 2018

Approved by

Lee, Phill-Seung
Professor of Mechanical Engineering

The study was conducted in accordance with Code of Research Ethics[1].

1) Declaration of Ethical Conduct in Research: I, as a graduate student of Korea Advanced Institute of Science and Technology, hereby declare that I have not committed any act that may damage the credibility of my research. This includes, but is not limited to, falsification, thesis written by someone else, distortion of research findings, and plagiarism. I confirm that my dissertation contains honest conclusions based on my own careful research under the guidance of my advisor.

MME 20173601

Choi, Hyunggyu. Hydroelastic analysis of floating structures subjected to underwater explosive bubbles. Department of Mechanical Engineering. 2019. 49+ Ⅴpages. Advisor: Lee, Phill-Seung. (Text in English)

Abstract

The coupled model for the interaction between an underwater explosive bubble and a floating structure is studied. During the violent expansion and collapse of the bubble, the explosive bubble deforms the structure. At the same time, the response of the structure affects the behavior of the bubble. In this study, the fluid domain for the bubble is modeled by using the boundary element method and the structure domain is modeled by using the finite element method. Based on the acceleration potential theory, we can construct a single set of coupled equations considering both the behavior of the bubble and the response of the structure simultaneously. In this study, we apply the quadratic surface fitting for constructing the coupled equation to avoid complex computation and weighted least square to minimize the error. To validate our model, we compare the results with both the rigid wall case and the free surface case. Then, the numerical example of steel plate is compared with LS-DYNA. Additionally, the change of the behavior of the bubble according to the stiffness of the plate is studied.

Keywords Boundary element method, Finite element method, Fluid – structure interaction, bubble dynamics, Hydroelastic analysis, Direct coupled method, Floating plate structures.

Contents

List of Tables

List of Figures

Chapter 1. introduction

Generally, the dynamic behavior of a floating structure has been considered as rigid motion because this assumption give acceptable results with simple and efficient analysis. However, if a floating structure experiences an extreme situation such as an underwater explosion, we have to consider a deformation of the floating structure. The underwater explosion is a complicated phenomenon. It generally consists of shock wave, bubble pulsation, and jet impact. Until now, lots of studies about underwater explosive bubble have been studied by using finite volume method, smoothed particle hydrodynamics, boundary element method, and so on [8,23]. Furthermore, the interaction between an underwater explosion bubble and a structure has been studied gradually [9,20,25].

Because of violent motion of the bubble caused by underwater explosion, the neighboring structure will be seriously deformed. At this moment, the structural deformation changes the shape of boundary and simultaneously affects the bubble's behavior. For this reason, the interaction between an underwater explosion and a structure has strong nonlinearity. In this extreme environment where the survivability of naval ships is important, we have to take the nonlinearity of the coupling effects into account.

There are some studies about interaction between bubble and structure. At first, using the spherical bubble model and elastic-plastic beam theory, the influence of spherical bubble pulse loads on a ship hull was studied [12]. The interaction between a bubble and a rigid movable structure has been studied [13]. Recently, some researchers have employed finite element method for structural part to study the interaction between a bubble and an elastic-plastic structure [14,25].

To predict a deformation of structure, we need to know the hydrodynamic force acting on the structure. In fluid-structure interaction problem, it is usually determined by integrating the pressure over the surface of structure. However, because of the nonlinear effects, it is quite difficult to compute the partial derivative of the potential with respect to time ϕ_t which is one of the Bernoulli equation terms to calculate pressure. Some researchers applied the finite difference method to compute ϕ_t [14,15,19]. However, this loosely coupled model using the finite difference method often results in numerical instabilities using the small time steps of bubble and the motion of the boundary. In present study, a completely coupled model for interaction between underwater explosion and a structure is studied using acceleration potential theory to calculate ϕ_t precisely [16]. Using this theory, we can decouple the mutual dependence of the hydrodynamic force and the structural response [25]. However, the exceedingly complex numerical calculation is needed to compute the coupled equation terms. Therefore, in this study, we apply the surface fitting and the weighted least square to calculation the coupled equation terms to avoid the complexity.

Fluid domain was assumed as an ideal fluid based on the assumption of irrotational, inviscid, and incompressible. Boundary element method is adopted to the fluid domain to calculate the velocity potential and the acceleration potential in the fluid domain. For the structural part, finite element method is adopted to the structural domain. we modeled the floating structure as shell structure, because most of the offshore structure or ships are almost made up of thin plate. Additionally, considering extension into the various shape of structure and the position of detonation, we implement fully three dimensional case.

Overall description of the problem and assumptions applied to solve bubble dynamics problem is in chapter 2. In this chapter, we derive governing equations and discretize the equations for fluid and some numerical scheme for the initial conditions, the boundary conditions and time step. In chapter 3, the MITC3 shell finite element is introduced to modeling a floating structure. Then, based on the acceleration potential theory, the coupled model for the interaction between the explosive bubble and the floating structure is derived. To validate our model, the results is compared with the two extreme cases in the plate stiffness. For the numerical example, a large steel plate is compared with LS-DYNA. Finally, the behavior of the explosive bubble depending on the flexural rigidity of the plate is studied.

Chapter 2. Background theory of the bubble dynamics

Before constructing coupled model for interaction between an underwater explosive bubble and nearby structure, some background theories for the bubble dynamics are introduced in this chapter, such as the boundary integral method, boundary conditions for a gas bubble, and Rayleigh-Plesset equation for initial conditions. In this study, the shock wave which last very short time is negligible. So we assumed that the fluid in solution domain is an ideal fluid, which means that the fluid is irrotational, inviscid, and incompressible. Based on this assumption, we can use the Laplace equation and transform the governing equation into a boundary only equation.

2.1. Boundary Integral equation

The fluid behavior near an explosive bubble is regarded as a potential flow because the flow induced by explosion has a high Reynolds number. So the potential flow assumes that the fluid in the solution domain is incompressible, inviscid, and irrotational. In this cases, we can define a velocity potential which satisfies the Laplace equation 2005. Using Green's 2nd theorem, the Laplace equation could be transformed into the boundary equation. This boundary integral approach has advantages in computational cost by reducing integral dimension and convenience for handling boundary surface between a gas bubble and fluid. Based on the ideal fluid assumption, the velocity potential satisfies the Laplace equation [2].

$$\nabla^2\varphi = \frac{\partial^2\varphi}{\partial x^2} + \frac{\partial^2\varphi}{\partial y^2} + \frac{\partial^2\varphi}{\partial z^2} = 0, \tag{2.1}$$

where ∇^2 is the Laplacian operator, φ is the velocity potential, and x, y, and z is Cartesian coordinate axis. To solve above differential equation, we define a Green function which satisfies the three dimensional Laplace equation as follows:

$$G(P,Q) = \frac{1}{|P-Q|} = \frac{1}{R_{PQ}}, \tag{2.2}$$

where P is a source point in the fluid domain, Q is a field point on the boundary of the fluid domain, and R_{PQ} is the distance between the source point P and the field point Q as shown in the Figure 2.1.

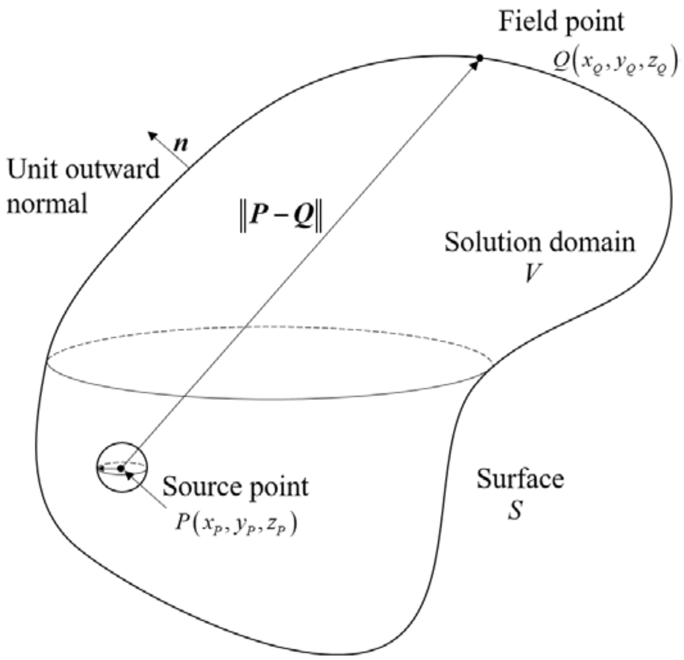

Figure 2.1 A three dimension domain with a boundary surface S, and a volume V. the point P and Q are a source point and a field point, respectively. The vector n is an outward unit normal vector on the boundary surface. An extremely small sphere is located at the source point to avoid the singularity during the formulation. The radius of the sphere becomes zero.

If the velocity potential and the Green function are continuous on the second derivatives, then we can transform the governing differential equation into an integral form based on Green's second identity.

$$\int_V (\varphi\nabla^2 G - G\nabla^2\varphi)dV = \int_S \left(\varphi\frac{\partial G}{\partial n} - G\frac{\partial\varphi}{\partial n}\right)dS\ , \tag{2.3}$$

where V is the volume of fluid domain, S is the surface of the fluid domain, and the direction of n is outward normal. Although the velocity potential always satisfies the Laplace equation because of the definition, the Green function doesn't satisfy the Laplace equation when the source point P and the field point Q are close to each other. To avoid this problem, we assume that there is an extremely small sphere with radius ρ and surface S_ρ at the source point P, and then get rid of the volume V_ρ in the fluid domain.

$$\int_{V-V_\rho} (\varphi\nabla^2 G - G\nabla^2\varphi)dV = \int_{S+S_\rho} \left(\varphi\frac{\partial G}{\partial n} - G\frac{\partial\varphi}{\partial n}\right)dS\ , \tag{2.4}$$

In the domain, both the velocity potential and the Green function always satisfies the Laplace equation.

So the left-hand side of above equation becomes zero. The remaining right-hand side of Eqn.(2.4) could be expressed as below,

$$\int_S \left(\varphi \frac{\partial G}{\partial n} - G \frac{\partial \varphi}{\partial n} \right) dS + \int_{S_\rho} \left(\varphi \frac{\partial G}{\partial n} - G \frac{\partial \varphi}{\partial n} \right) dS = 0 , \tag{2.5}$$

Then depending on the definition of a small sphere, the second term of Eqn.(2.5) becomes,

$$\int_{S_\rho} \left(\varphi \frac{\partial G}{\partial n} - G \frac{\partial \varphi}{\partial n} \right) dS = \int_0^\pi \left(\varphi \frac{\partial G}{\partial n} - G \frac{\partial \varphi}{\partial n} \right) 2\pi\rho^2 \sin\theta \, \mathrm{d}\theta , \tag{2.6}$$

where θ is the anticlockwise angle at source point P based on the polar coordinate. Because the distance between the source point P and the field point Q becomes ρ in this case and the direction of outward normal is equal to the direction from field point Q to source point P, the equation becomes

$$\int_{S_\rho} \left(\varphi \frac{\partial G}{\partial n} - G \frac{\partial \varphi}{\partial n} \right) dS = \int_0^\pi \left(\varphi(P) \left(\frac{1}{\rho^2} \right) - \left(\frac{1}{\rho} \right) \frac{\partial \varphi(P)}{\partial n} \right) 2\pi\rho^2 \sin\theta \, \mathrm{d}\theta , \tag{2.7}$$

If we take the limit on the equation as ρ approaches zero, this equation becomes

$$2\pi\varphi(P) \int_0^\pi \sin\theta \, \mathrm{d}\theta = 4\pi\varphi(P) , \tag{2.8}$$

After substituting Eqn.(2.8) into Eqn.(2.5), we can get the final form of governing equation integral forms as follows:

$$4\pi\varphi(P) = \int_S \left(G(P,Q) \frac{\partial \varphi(Q)}{\partial n} - \varphi(Q) \frac{\partial G(P,Q)}{\partial n} \right) dS , \tag{2.9}$$

Because we only need to values on the boundary of the domain, we take the case that the source point P is on the boundary. Then the final form of the boundary integral equation becomes

$$C(P)\varphi(P) = \int_S \left(G(P,Q) \frac{\partial \varphi(Q)}{\partial n} - \varphi(Q) \frac{\partial G(P,Q)}{\partial n} \right) dS , \tag{2.10}$$

where C is solid angle which is a geometrical parameter defined as the ratio of the fluid area to the spherical area. The solid angle on the bubble surface which is close can be calculated indirectly [4]. However, when considering the free surface, we have to calculate the solid angle directly.

2.2. Boundary conditions on the surface

At all the boundary which is free to move, the motion of the fluid particle should satisfy certain conditions. These conditions on the motion of the fluid particle is a kinematic boundary condition. In this study, we assumed that the fluid is an ideal fluid which means irrotational, inviscid, and incompressible. Therefore, based on the definition of the velocity potential, we can define the kinematic boundary condition.

$$\mathbf{v} = \nabla\varphi \quad \text{on the } S_f \text{ and } S_b, \tag{2.11}$$

where $\mathbf{v}$ is the velocity of the fluid. The surface S_f and S_b are the free surface and the bubble surface as shown in the Figure 2.2. Besides the kinematic boundary conditions, there are the dynamic boundary conditions which mean the balance of the pressure at the boundary surface [22].

Depending on the potential flow, we can use the unsteady Bernoulli equation for calculating the pressure

$$p_f = p_{atm} - \rho\frac{\partial\varphi}{\partial t} - \frac{1}{2}\rho\left|\nabla\varphi\right|^2 - \rho g z_f \quad \text{on the } S_f, \tag{2.12}$$

$$p_b = p_{atm} - \rho\frac{\partial\varphi}{\partial t} - \frac{1}{2}\rho\left|\nabla\varphi\right|^2 - \rho g z_b \quad \text{on the } S_b, \tag{2.13}$$

where the subscript f and b means the free surface and the bubble surface and the z, p_{atm}, ρ, and g are a position of the fluid, atmospheric pressure, fluid density, and gravitational acceleration.

The p_f and p_b are the pressure at the free surface and the bubble surface which is given by,

$$p_f = p_{atm} \quad \text{on the } S_f, \tag{2.14}$$

$$p_b = p_v + p_g \quad \text{on the } S_b, \tag{2.15}$$

where the p_v and p_g are the vapor pressure and the gas pressure of the bubble. In this study, p_v is zero. The gas pressure can be obtained by assuming that the process is adiabatic.

$$p_g = p_{g0}\left(\frac{V_0}{V_b}\right)^{\lambda}, \tag{2.16}$$

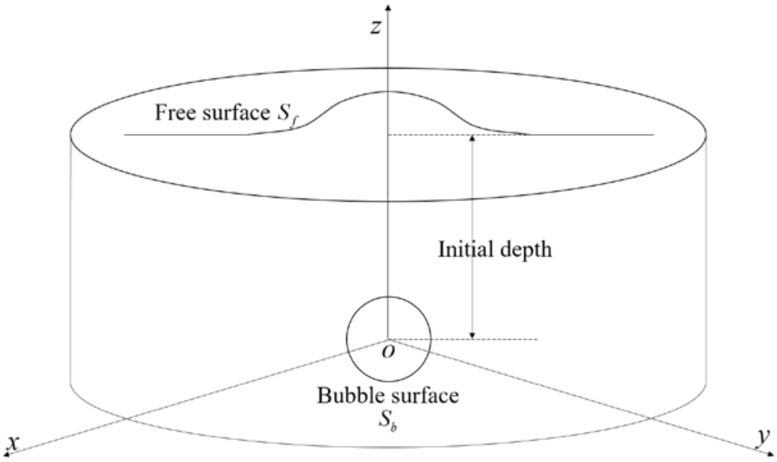

Figure 2.2 A three dimensional solution domain and the global Cartesian coordinate is shown. Sb and Sf are the boundary surface for the bubble and the boundary surface of the free surface. The origin is located at the center of the bubble and the initial position of the bubble is given by initial depth length.

where p_{g0}, V_0, and V_b are the initial gas pressure inside the bubble, the initial volume of the bubble and the volume of the bubble at each time step. λ is the specific heat ratio. In this study, the value of the specific heat ratio is 1.25 which is for an explosion of TNT material.

By substituting Eqs.(2.14), (2.15), and (2.16) into Eqs.(2.12) and (2.13), the relation between the Bernoulli equation and the balance of the pressure become

$$\rho \frac{\partial \varphi}{\partial t} = -\frac{1}{2}\rho \left|\nabla \varphi\right|^2 - \rho g z_f \quad \text{on the } S_f, \tag{2.17}$$

$$\rho \frac{\partial \varphi}{\partial t} = p_{atm} - p_{g0}\left(\frac{V_0}{V_b}\right)^{\lambda} - \frac{1}{2}\rho \left|\nabla \varphi\right|^2 - \rho g z_b \quad \text{on the } S_b, \tag{2.18}$$

To update the shape of the free surface and the bubble surface, we need to calculate the material derivative of the velocity potential not the partial derivative of the velocity potential with respect to time. Because the velocity potential is a function not only time but also position. From both the definition of the material derivative and the velocity potential, the relation between the material derivative and the partial derivative with respect to time of the velocity potential is given by.

$$\frac{\partial \varphi}{\partial t} = \frac{d\varphi}{dt} - \nabla\varphi \cdot \nabla\varphi \,, \tag{2.19}$$

By substituting Eqn.(2.19) into Eqns.(2.17) and (2.18), the final form of the dynamic boundary conditions can be obtained.

$$\frac{d\varphi}{dt} = \frac{1}{2}\left|\nabla\varphi\right|^2 - gz_f \quad \text{on the} \quad S_f \,, \tag{2.20}$$

$$\frac{d\varphi}{dt} = \frac{p_{atm}}{\rho} - \frac{p_{g0}}{\rho}\left(\frac{V_0}{V_b}\right)^{\lambda} + \frac{1}{2}\left|\nabla\varphi\right|^2 - gz_b \quad \text{on the} \quad S_b \,, \tag{2.21}$$

Finally, we can update the deformation of the boundary surface by using the kinematic boundary condition, Eqn.(2.11), which means the shape of the free surface and the bubble surface. Additionally, we can update the velocity potential by using the dynamic boundary conditions, Eqns.(2.20) and (2.21) at each surface.

2.3. Initial conditions of an explosive bubble

In analysis of time domain, we have to know initial conditions of the solution domain. Because the free surface is steady state at the beginning, the initial value of the velocity potential is zero naturally. However, it is not easy to know the exact initial conditions of an explosive bubble. Therefore, we need to make some assumptions on the bubble shape, the inside pressure, and the velocity potential at the beginning of the simulation. In the case of the gas bubble, it is well known that the behavior of the gas bubble follows the Rayleigh-Plesset equation, if the gravitational acceleration is negligible. Therefore, if we assume the initial shape of the bubble is spherical, then we can obtain the initial shape of the bubble by using the Rayleigh-Plesset equation [7].

Based on the assumption of the incompressible fluid and no gravity which means that the bubble is always spherical because there is no buoyancy, the Rayleigh-Plesset equation can be derived. From the mass conservation in the fluid domain, the velocity of the fluid particle can be obtained.

$$\dot{r}(r,t) = \frac{dR_b}{dt}\frac{{R_b}^2}{r^2} \,, \tag{2.22}$$

where $\dot{r}$, r are the radial velocity of the fluid particle and the position of the fluid particle, and R_b is the radius of the bubble. Therefore, r should be larger than the R_b as shown in the Figure 2.3. If the inviscid is additionally assumed, the Navier-Stokes equation can be expressed as follows in the spherical coordinate.

$$\frac{\partial \dot{r}}{\partial t}+\dot{r}\frac{\partial \dot{r}}{\partial r}=-\frac{1}{\rho}\frac{\partial p}{\partial r}, \tag{2.23}$$

where p is the pressure of the fluid. After substituting the Eq.(2.22) into the Eq.(2.23), integrate the equation with respect to r then the equation becomes

$$\frac{d^2R}{dt^2}\frac{R^2}{r}+2\left(\frac{dR}{dt}\right)^2\left[\frac{R}{r}-\frac{R^4}{4r^4}\right]=\frac{p(r,t)-p_\infty}{\rho}, \tag{2.24}$$

where p_∞ is the pressure of the far from the bubble.

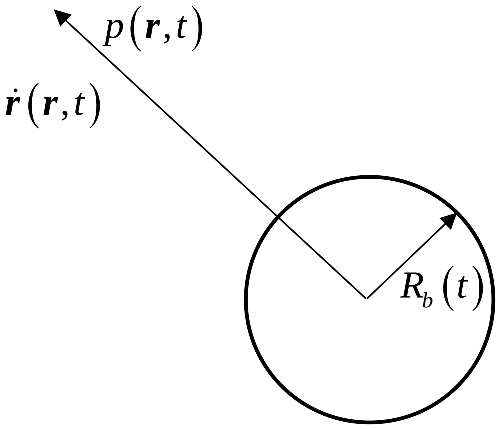

Figure 2.3 Based on the assumption of a spherical bubble, the schematic configuration of the derivation for the Rayleigh – Plesset equation is shown. P(r,t) and r(r,t) are the pressure and the velocity of the fluid particle at the position r. Rb(t) is the instantaneous radius of the spherical bubble.

When considering the interface between the bubble and the fluid, it means that $r = R$, and the pressure $p(r,t)$ becomes $p_b(t)$. Thus, finally, the Rayleigh-Plesset equation is obtained.

$$\rho\left[R\frac{d^2R}{dt^2}+\frac{3}{2}\left(\frac{dR}{dt}\right)^2\right]=p_b(t)-p_\infty, \tag{2.25}$$

where R is the instantaneous radius of the bubble. After multiplying $2R\dot{R}$ on both sides, the above equation can be integrated analytically. Although the radial velocity is not zero because of the high pressure of the bubble, it is set to zero for the numerical calculation. Then, the relation between the initial radius of the bubble and the initial pressure of the inside bubble can be obtained.

$$\frac{P_{g0}}{P_{\infty}(\lambda-1)}\left(R_0^{3\lambda}-R_0^3\right)=R_0^3-1, \tag{2.26}$$

To determine the initial radius of the bubble, we need to know the initial pressure of the bubble. There is an empirical formula between the initial gas pressure of the explosive bubble and the weight of TNT which is found by Cole.

$$p_{g0}=1.39\times10^5\left(\frac{W}{V_0}\right)^{\lambda}, \tag{2.27}$$

where W is the weight of the TNT material. From above formula, we can obtain the initial gas pressure of the bubble. Because the relation between the initial radius and the initial gas pressure of the bubble are not independent, those values are need to be determined considering both Eqn.(2.26) and Eqn.(2.27)

2.4. Numerical modeling

In this chapter, the boundary surface of the fluid domain is discretized for the numerical calculation using the three node linear triangular elements and then the boundary integral equation is transformed into the matrix form of the algebraic equations. A single bubble which is initially sphere is considered and is modeled by icosahedron which has no preference for any direction as shown in Figure 2.4 [3]. In consideration of the expandability into the interaction with the offshore structures which are having an arbitrary shape, we implement the code as the fully three dimensional case. Besides the discretization, some numerical schemes are introduced such as how to determine the direction of normal vector, and the tangential velocity at each node, and how to determine the time step, etc.

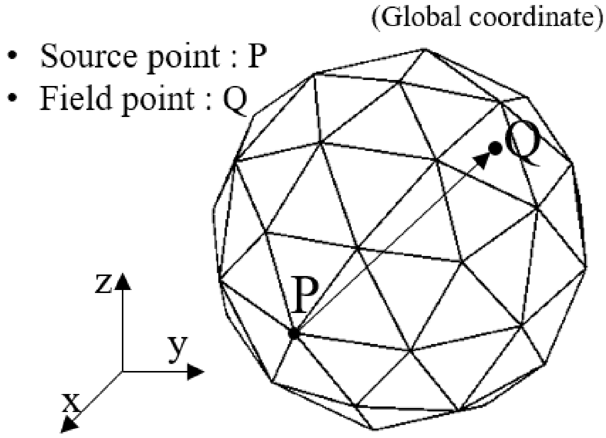

Figure 2.4 The discretized bubble surface. For non-preference for any direction, the icosahedron is used for mesh. The initial shape of the bubble is assumed as spherical., 642 nodes for the bubble surface is used.

After discretizing the boundary surface into some elements using a linear triangular element, the governing boundary integral equation, Eqn.(2.10), also needs to be discretized. The Eqn.(2.10) can be expressed as the summation of the integration over each element.

$$C(P_i)\varphi(P_i)+\sum_{j=1}^{N_e}\left[\int_{S_j}\frac{\partial G(P_i,Q)}{\partial n}\varphi(Q)\,dS\right]=\sum_{j=1}^{N_e}\left[\int_{S_j}\frac{\partial \varphi(Q)}{\partial n}G(P_i,Q)\,dS\right],\quad i=1,2,...,N, \tag{2.28}$$

where N_e and N are the number of the elements and the nodes, P_i is the position of the ith source point, and S_j means the surface of jth element. The integration over each element in the square bracket should be transformed into the local coordinate for the numerical calculation. Therefore, the area coordinate is used for the three node triangular element and the interpolation for the geometry, potential, the normal derivative of the potential can be expressed as follows.

$$\begin{aligned}&\boldsymbol{x}=(1-r-s)\,\boldsymbol{x}_A+r\boldsymbol{x}_B+s\boldsymbol{x}_C,\\&\varphi=(1-r-s)\varphi_A+r\varphi_B+s\varphi_C,\\&\varphi_n=(1-r-s)\varphi_{n,\mathrm{A}}+r\varphi_{n,\mathrm{B}}+s\varphi_{n,\mathrm{C}},\end{aligned} \tag{2.29}$$

where $\boldsymbol{x}$ and φ_n are the position vector and the normal derivative of the potential. The values with subscript A, B, and C are the vertex value of the triangle as shown in Figure 2.5.

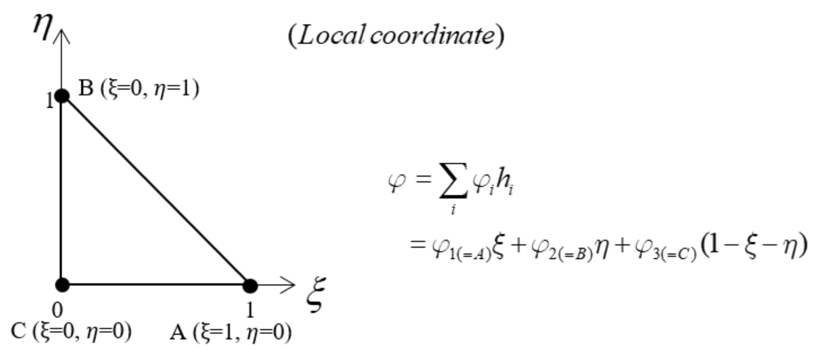

Figure 2.5 The local area coordinate for the three node triangular element and the shape function are shown. The values inside the element is obtained by the nodal values based on the linear interpolation.

Substituting above interpolation into the integration in Eqn(2.28), the first and the second integration term in the square bracket can be expressed as follows.

$$\begin{aligned}\hat{H} &= \int_S \frac{\partial G(P,Q)}{\partial n}\varphi(Q)\,dS = \int_0^1\int_0^{1-s} \frac{\boldsymbol{n}\cdot(\boldsymbol{x}-\boldsymbol{x}_P)}{R^3}\big((1-r-s)\varphi_A + r\varphi_B + s\varphi_C\big)Jdrds \\ &= \varphi_A\hat{H}_1 + \varphi_B\hat{H}_2 + \varphi_C\hat{H}_3\end{aligned}, \tag{2.30}$$

$$\begin{aligned}G &= \int_S \frac{\partial\varphi(Q)}{\partial n}G(P,Q)dS = \int_0^1\int_0^{1-s} \frac{(1-r-s)\varphi_{n,A} + r\varphi_{n,B} + s\varphi_{n,C}}{R}Jdrds \\ &= \varphi_{n,A}G_1 + \varphi_{n,B}G_2 + \varphi_{n,C}G_3\end{aligned}, \tag{2.31}$$

where $\boldsymbol{n}$, J, and R is the outward normal vector, the determinant of the jacobean and the distance between the source point P and the field point. The discretized integral equation can be expressed as matrix form.

$$C(P_i)\varphi(P_i) + \sum_{j=1}^{N_e}\hat{H}_{ij}\varphi_j = \sum_{j=1}^{N_e}G_{ij}\varphi_{n,j}, \quad i = 1,2,\ldots,N, \tag{2.32}$$

To simplify above matrix form, define the relation between the solid angle and the influence coefficients matrix $\hat{H}$ as below.

$$H_{ij} = \hat{H}_{ij} + C(P_i)\delta_{ij}, \tag{2.33}$$

where δ_{ij} is Dirac delta function. Finally, the boundary integral equation in the matrix form can be obtained.

$$\mathbf{H}\boldsymbol{\varphi} = \mathbf{G}\boldsymbol{\varphi}_n, \tag{2.34}$$

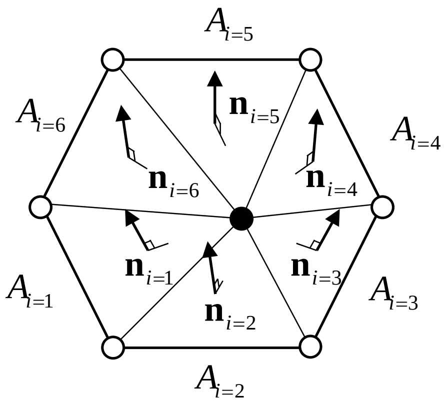

Figure 2.6 The *i*th node with the black point and the local configuration of the surrounding elements are shown. The outward unit normal vector is approximated by the weighted average using the normal vectors of surrounding element. The weight is an inverse of an element area.

We can get the normal velocity on the boundary surface by solving the matrix equation. Although we know the normal velocity at each node now, the direction of the normal vector at each node is still unknown. Furthermore, the tangential velocity and its direction should be determined.

In order to determine the direction of the normal vector at the node, we use weighted average by using an area of surrounding element as shown in Figure 2.6, because there is no mathematically exact solution for the discretized boundary surface [5].

$$\mathbf{n} = \frac{\sum_{i=1}^{N_{sur}} \frac{\mathbf{n}_i}{A_i}}{\sum_{i=1}^{N_{sur}} \frac{1}{A_i}}, \tag{2.35}$$

where N_{sur} is the number of the surrounding element at each node. A_i and $\mathbf{n}_i$ are the area and the normal vector of the *i*th element surrounding the node. Because a smaller element gives a more accurate estimation on the local properties than a larger element, the weighting function is an inverse of the area[2001zhang]. In the same way, we can obtain the tangential velocity vector at a node.

$$\mathbf{v} = \frac{\sum_{i=1}^{N_{sur}} \frac{\mathbf{v}_i}{A_i}}{\sum_{i=1}^{N_{sur}} \frac{1}{A_i}}, \tag{2.36}$$

where $\mathbf{v}_i$ is the tangential velocity of the surrounding element at a node. The tangential velocity of an element can be obtained using the finite difference method as shown in Figure 2.7.

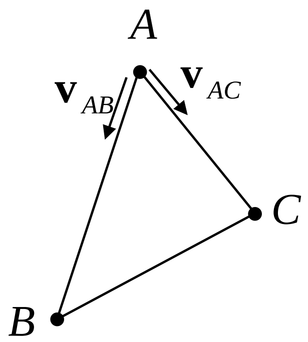

Figure 2.7 The tangential velocity of an element and its direction are shown. The magnitude of the velocity along each direction is obtained by the finite difference method and the direction of the velocity is obtained by the edge points in accordance with the calculation of the velocity.

$$\boldsymbol{v}_{AB} = \frac{\partial \varphi_{AB}}{\partial l_{AB}} = \frac{\varphi_B - \varphi_A}{\left|\boldsymbol{x}_B - \boldsymbol{x}_A\right|}, \ \boldsymbol{v}_{AC} = \frac{\partial \varphi_{AC}}{\partial m_{AC}} = \frac{\varphi_C - \varphi_A}{\left|\boldsymbol{x}_C - \boldsymbol{x}_A\right|} \tag{2.37}$$

where l and m is the direction vector of the tangential velocity which is defined by along the edge line of the triangle. Depending on the equations from Eqn.(2.34) to Eqn.(2.37), we can determine the velocity at a node on the boundary surface. However, the velocity is expressed as local component based on the normal and the tangential vector. We need to transform the component into the global coordinate to update the shape of the boundary.

$$\mathbf{v} = \begin{bmatrix} v_x \\ v_y \\ v_z \end{bmatrix} = \begin{bmatrix} n_x & n_y & n_z \\ l_x & l_y & l_z \\ m_x & m_y & m_z \end{bmatrix}^{-1} \begin{bmatrix} \varphi_n \\ \varphi_l \\ \varphi_m \end{bmatrix}, \tag{2.38}$$

After obtaining the velocity in the global coordinate, we can update the shape of the boundary surface in accordance with the kinematic boundary conditions in chapter 2.2. In this study, we adopt the Runge-Kutta 4th order method for time integration in the bubble dynamics and the Euler forward method in the bubble-structure interaction problem.

2.5. Results

Because of the complexity of the underwater explosion which consists of various phenomena including shock wave, pulsation, and jet impact, it is not easy to experiment the large scale explosion. Therefore, we simulate the small scale explosion to verify implemented code by comparison with previous and the experiment results. The behavior of an explosive gas bubble near the rigid wall is compared with previous study [1] and the behavior of an explosive gas bubble under the free surface is compared with experiments results.

2.5.1. Comparison with previous study

The bubble shape as a function of time under the different distance from the rigid wall and the effect of the buoyancy is compared with previous study. To consider the rigid wall, we adopt the mirror source technique which uses the reflected image of the explosive bubble[6]. The domain and the schematic configuration are shown in Figure 2.8. The distance from the rigid wall and the buoyancy are non-dimensionalized [1,11].

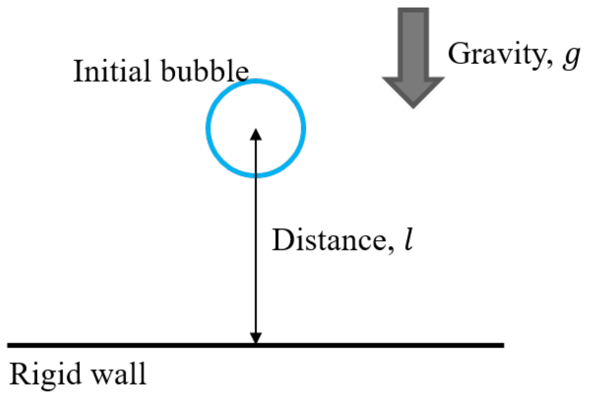

Figure 2.8 The schematic configuration shows the initial position from the rigid wall and the gravity.

$$\gamma = \frac{h}{R_m}, \quad \delta = \sqrt{\frac{\rho g R_m}{p_\infty}}, \tag{2.39}$$

where h and R_m is the initial depth of the detonation and the maximum radius of the bubble. the bubble behaves variously depending on the distance from the nearby rigid wall and the buoyancy as shown.

Table 2.1 Initial depth and buoyancy parameters for each case

Case		1	2	3	4	5	6
Parameter	γ	2.0	1.0	2.0	2.0	1.0	1.0
	δ	-	-	0.316	-0.316	0.224	0.447

Case 1 and 2 are the comparison under the initial depth when there is no buoyancy. Case 3 and 4 are the comparison under the direction of the buoyancy when the initial depth is same. Finally, case 5 and 6 are comparison under the magnitude of the buoyancy when the others are in same conditions. From Figure 2.9 to Figure 2.14, left figure (a) shows the previous bubble dynamics results in axialsymmerty case and the right figure (b) show the implemented codes results in three dimensional case.

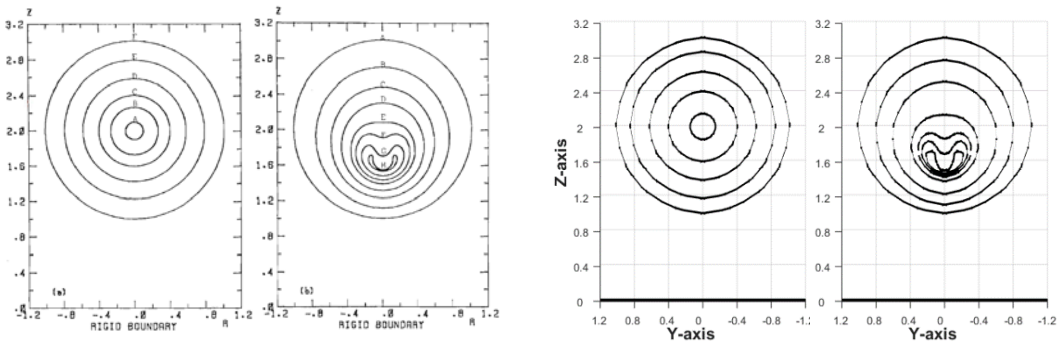

(a) (b)

Figure 2.9 Bubble dynamics results for $\gamma = 2.0$, $\delta = 0$ in case 1.

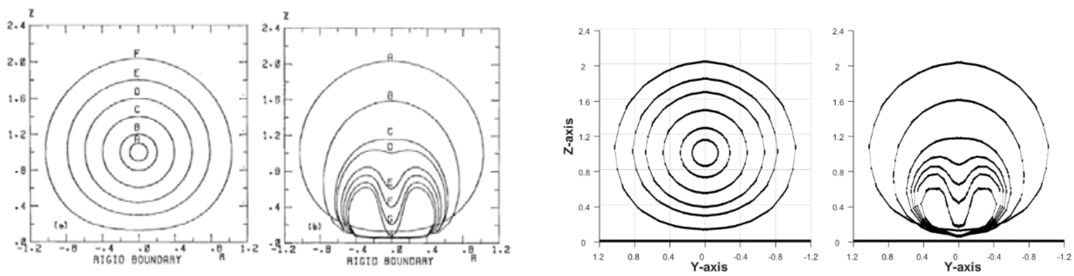

(a) (b)

Figure 2.10 Bubble dynamics results for $\gamma = 1.0$, $\delta = 0$ in case 2.

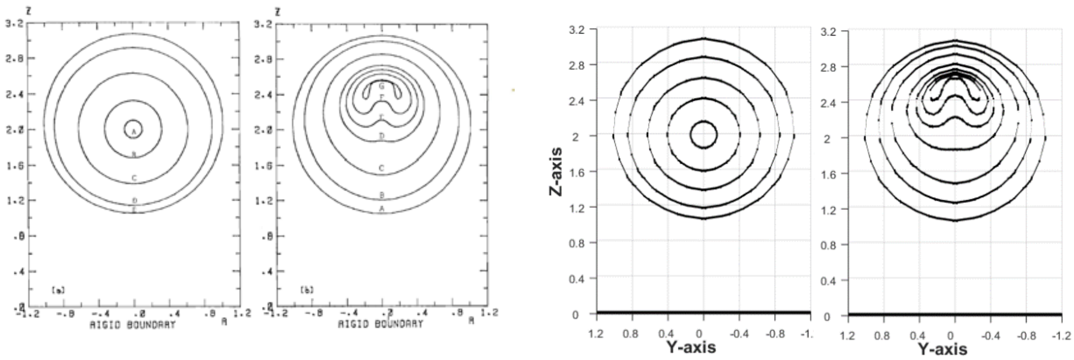

(a) (b)

Figure 2.11 Bubble dynamics results for $\gamma = 2.0$, $\delta = 0.316$ in case 3.

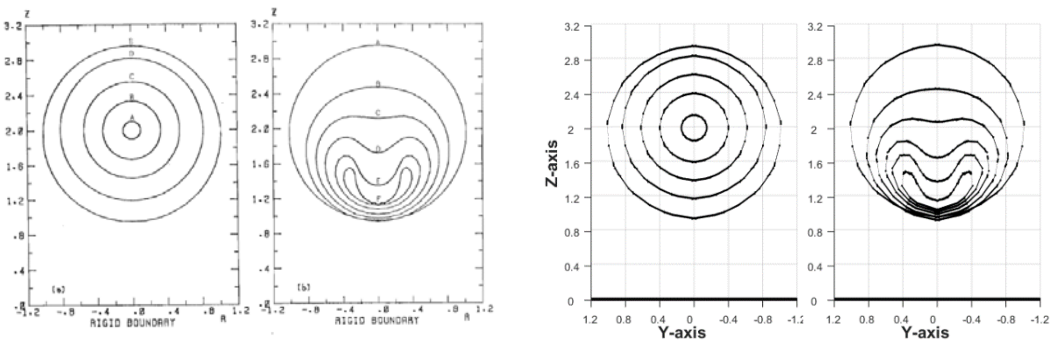

(a) (b)

Figure 2.12 Bubble dynamics results for $\gamma = 2.0$, $\delta = -0.316$ in case 4.

The bubble expands maintaining the spherical shape at the beginning. Then, it loses its spherical shape and the bottom surface is flattened when the initial distance from the rigid wall is small. The axialsymmetry results and the three dimensional results are in general agreement. As shown in the Figure 2.9 and Figure 2.10, the closer the wall is, the stronger collapse which forms the jet flow occurs from the case 1 and case2. When the initial distance and the direction of the gravity are same, the jet flow direction can change depending on the direction of the gravity from the case 3 and case 4 as shown in Figure 2.11 and Figure 2.12. Although the initial distance and the direction of the gravity are same in case 5 and case 6, the behavior of the bubble moves in the opposite direction at each other because of the magnitude of the gravity.

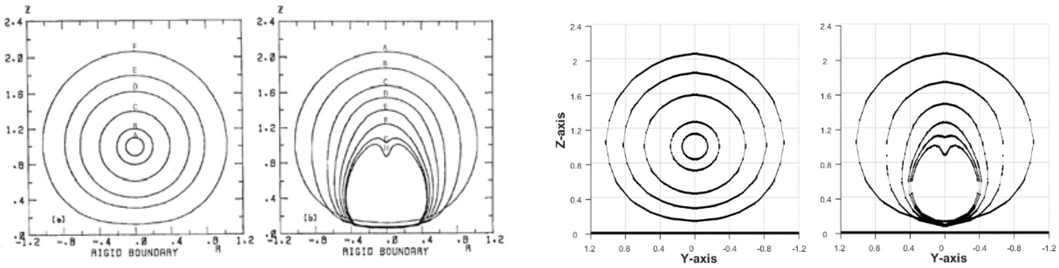

(a) (b)

Figure 2.13 Bubble dynamics results for $\gamma = 1.0$, $\delta = 0.224$ in case 5.

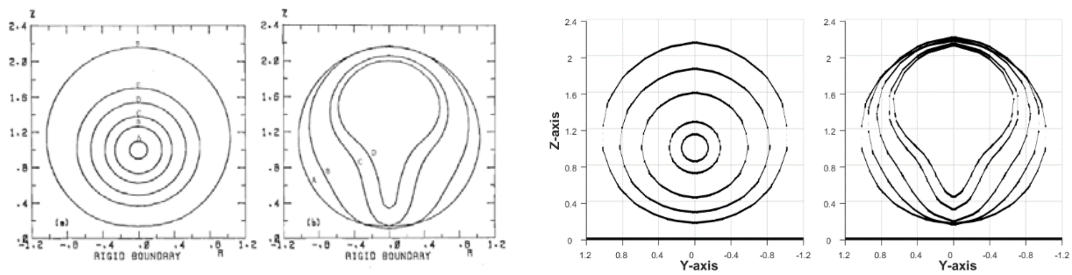

(a) (b)

Figure 2.14 Bubble dynamics results for $\gamma = 1.0$, $\delta = 0.447$ in case 6.

2.5.2. Comparison with experiment

An experiment with small scale underwater experiment is conducted to observe the behavior of an explosive gas bubble and the deformation of the free surface. The experiment is carried out in a tank with 10mm thick steel plate as shown in Figure 2.8. The charge weight of the Pentolite is 7.5g which is equivalent to 9.975g of TNT. The position of an explosive is the center of the tank and the depth is 0.25m from the free surface. The high speed camera is used to observe the bubble. The bubble and free surface shape at given time are shown in Figure 2.15.

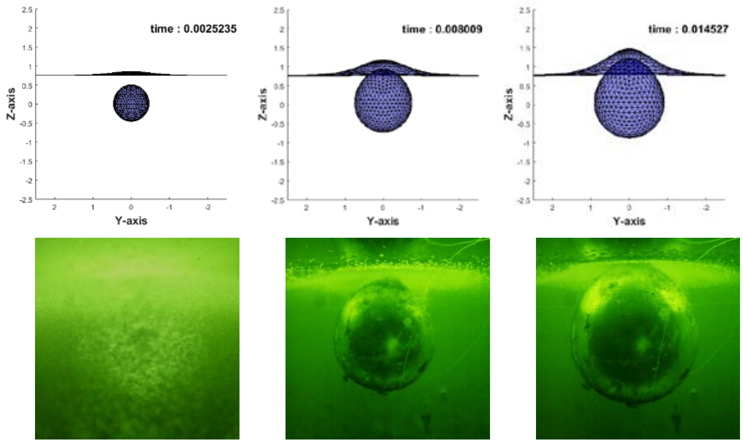

(a)

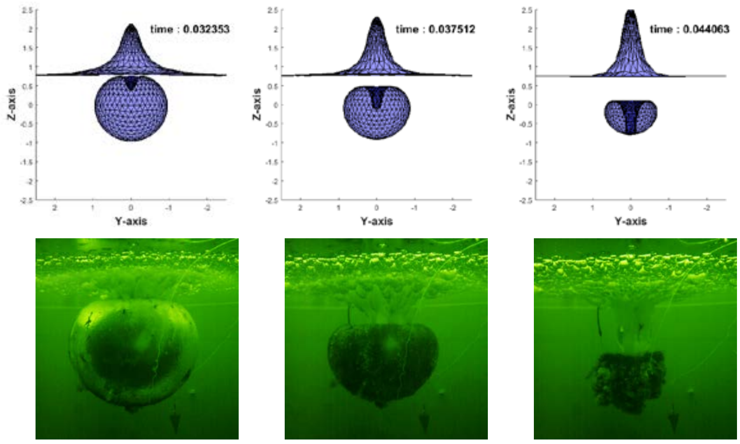

(b)

Figure 2.15 Comparison between bubble dynamics under the free surface and the experiment. (a) is for the expansion and (b) is for the collapse.

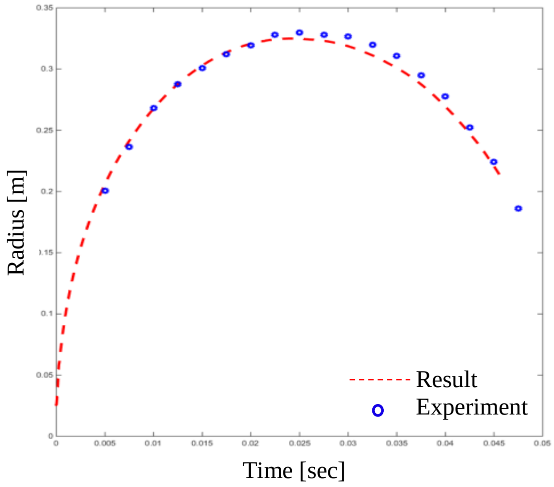

Figure 2.16 Time history of the bubble radius compared with experiment.

The Figure 2.15 (a) and (b) show the behavior of the bubble at the expansion and the collapse, respectively. Under the influence of the deformation of the free surface, the bubble shape is elongated along the z direction. When the bubble reaches its maximum volume, the upper part of the bubble is positioned above initial free surface as shown in Figure 2.15 (a). Then, it starts to collapse moving downward while the center of the free surface continues to elevate as shown in Figure 2.15 (b). The maximum radius from the experiment and the result are 0.3297m and 0.3349m, respectively and the period of the bubble are 0.0475sec and 0.0469sec, respectively as shown in Figure 2.16.

The results in this chapter will be used to validate the implemented codes for the coupled model for the interaction between an explosive bubble and a floating plate. Because the floating plate could be regarded as rigid wall and the free surface, depending on the stiffness of the plate, the two extreme cases in the stiffness of the plate are compared with the rigid wall case and the free surface case, respectively.

Chapter 3. Interaction between an underwater explosive bubble and a floating structure

We construct a coupled model for the interaction between an underwater explosive bubble and a floating structure to analysis the transient response of the structure. Because most of the offshore structure or the ships are made of thin plate shape, we modeled the floating structure as shell structure using finite element method. The fluid domain is modeled using boundary element method as mentioned in chapter 2. In the interaction problem, to accurately predict the deformation of the structure, the hydrodynamic force acting on the structure should be precisely computed. In this study, we adopt the acceleration potential theory to obtain the hydrodynamic pressure action on the structure surface simultaneously considering both the bubble dynamics and the response of the structure [16, 25]. The schematic configuration is shown in Figure 3.1.

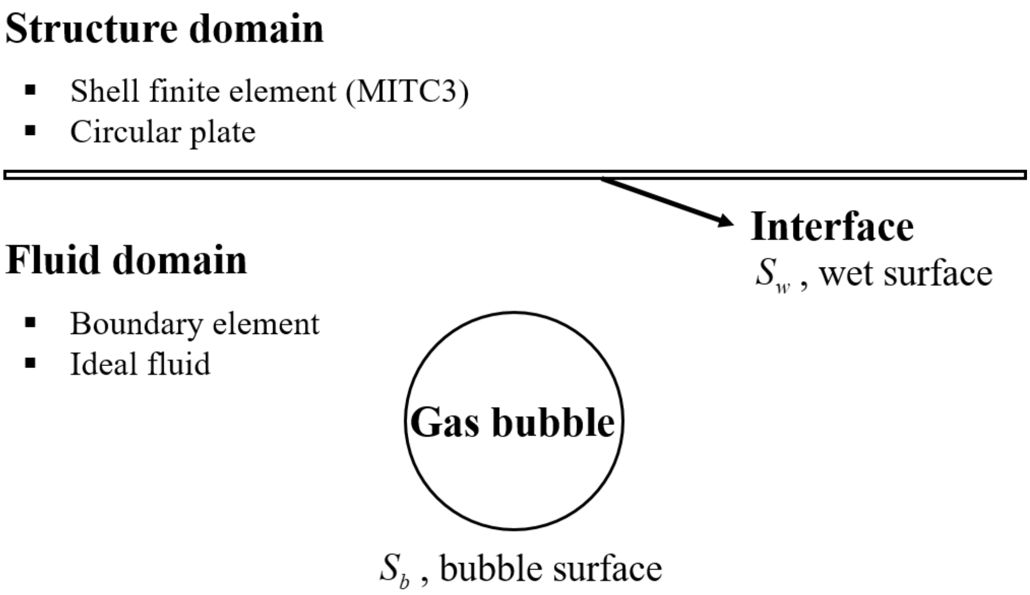

Figure 3.1 The schematic configuration for the interaction between an underwater explosive bubble and a floating structure. The gas bubble is modeled by using the boundary element method and the structure is modeled by using the finite element method. Based on the acceleration potential theory, the coupled model is constructed and the partial derivative of the velocity potential is directly calculated.

3.1. Shell element for the structure

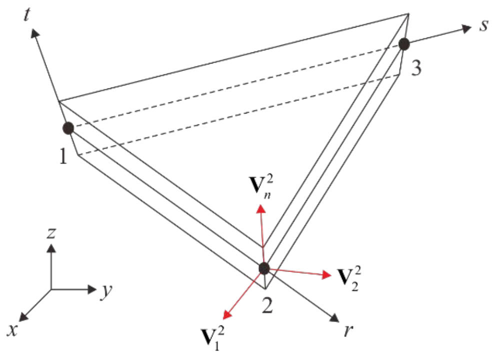

Figure 3.2 A continuum mechanics based finite shell element for the three node triangular element is shown. The nodes are located at the mid surface and the values inside the element are interpolated by using the nodal values

The fundamental assumption of the shell element is that there is no deformation along the thickness direction which is normal to the mid-surface of the structure. The geometry of a three node shell element is shown in Figure 3.2. Based on the isoparametric finite element procedure which means that the same shape functions are used for the interpolation for coordinate and the displacement, an arbitrary point within the element can be interpolated by

$$\mathbf{x}(r,s,t)=\sum_{i=1}^{3}h_i(r,s)\mathbf{x}_i+\frac{t}{2}\sum_{i=1}^{3}a_ih_i(r,s)\mathbf{V}_n^i \quad \textit{with} \quad h_1=1-r-s,\ h_2=r,\ h_3=s, \tag{3.1}$$

where $\mathbf{x}_i$ is the nodal position vector at the global Cartesian coordinate system and h_i is the two dimensional shape function for the standard isoparametric procedure to the *i*th node. $\mathbf{V}_n^i$ is the director vector and a_i is the thickness of the shell.

Based on the same shape function, the displacement interpolation can be obtained by

$$\mathbf{u}(r,s,t)=\sum_{i=1}^{3}h_i(r,s)\mathbf{u}_i+\frac{t}{2}\sum_{i=1}^{3}a_ih_i(r,s)\left(-\alpha_i\mathbf{V}_2^i+\beta_i\mathbf{V}_1^i\right), \tag{3.2}$$

where $\mathbf{u}_i$ is the *i*th nodal displacement vector, α_i and β_i are the rotations of the director vector $\mathbf{V}_2^i$ and $\mathbf{V}_1^i$, respectively. The director vector is defined by

$$\mathbf{V}_1^m \equiv \frac{\mathbf{e}_2 \times \mathbf{V}_n^m}{\left|\mathbf{e}_2 \times \mathbf{V}_n^m\right|}, \quad \mathbf{V}_2^m \equiv \mathbf{V}_n^m \times \mathbf{V}_1^m \quad , \tag{3.3}$$

The covariant components of the infinitesimal strain tensor is given by

$$e_{ij} = \frac{1}{2}\left(\mathbf{g}_i \cdot \mathbf{u}_{,j} + \mathbf{g}_j \cdot \mathbf{u}_{,i}\right), \tag{3.4}$$

where $\mathbf{g}$ is the covariant base vector of the natural curvilinear coordinate.

$$\mathbf{g}_i = \frac{\partial \mathbf{x}}{\partial r_i}, \ \mathbf{u}_{,i} = \frac{\partial \mathbf{u}}{\partial r_i}, \quad with \ \ r_1 = r, \ r_2 = s, \ r_3 = t \ , \tag{3.5}$$

The corresponding contravariant base vector should satisfy the relationships:

$$\mathbf{g}_i \cdot \mathbf{g}^j = \delta_{ij} \ , \tag{3.6}$$

where δ_{ij} is the Kronecker delta function. To satisfy the basic assumption that there is no stress along the thickness, we introduce the local Cartesian coordinate system and construct the constitutive matrix which has zero value at the component relevant to the thickness direction.

$$\mathbf{C} = \frac{E}{1-\nu^2}\begin{bmatrix} 1 & \nu & 0 & 0 & 0 & 0 \\ \nu & 1 & 0 & 0 & 0 & 0 \\ 0 & 0 & 0 & 0 & 0 & 0 \\ 0 & 0 & 0 & \frac{1-\nu}{2} & 0 & 0 \\ 0 & 0 & 0 & 0 & k\frac{1-\nu}{2} & 0 \\ 0 & 0 & 0 & 0 & 0 & k\frac{1-\nu}{2} \end{bmatrix}, \tag{3.7}$$

where $\mathbf{C}$ is the constitutive matrix in local Cartesian coordinate system. E , ν , and k are the Young's modulus and the Poisson 's ratio, and the shear correction factor. In this study, the shear correction factor is one. Because the constitutive matrix and the strain tensor are defined in different coordinate system, we should transform one of them into the other. The local Cartesian base vectors are defined by

$$\mathbf{e}_{\bar{r}} = \frac{\mathbf{g}_1 \times \mathbf{g}_3}{\left|\mathbf{g}_1 \times \mathbf{g}_3\right|}, \quad \mathbf{e}_{\bar{s}} = \frac{\mathbf{g}_3 \times \mathbf{e}_{\bar{r}}}{\left|\mathbf{g}_3 \times \mathbf{e}_{\bar{r}}\right|}, \quad \mathbf{e}_t = \frac{\mathbf{g}_3}{\left|\mathbf{g}_3\right|} \ , \tag{3.8}$$

The transformation matrix between the local Cartesian coordinate and the global Cartesian coordinate is given by

$$\mathbf{R} = \begin{bmatrix} \mathbf{e}_1 \cdot \mathbf{e}_{\bar{r}} & \mathbf{e}_1 \cdot \mathbf{e}_{\bar{s}} & \mathbf{e}_1 \cdot \mathbf{e}_t \\ \mathbf{e}_2 \cdot \mathbf{e}_{\bar{r}} & \mathbf{e}_2 \cdot \mathbf{e}_{\bar{s}} & \mathbf{e}_2 \cdot \mathbf{e}_t \\ \mathbf{e}_3 \cdot \mathbf{e}_{\bar{r}} & \mathbf{e}_3 \cdot \mathbf{e}_{\bar{s}} & \mathbf{e}_3 \cdot \mathbf{e}_t \end{bmatrix}, \tag{3.9}$$

Based on above relationship, we can transform the component of the constitutive matrix or the strain into each other.

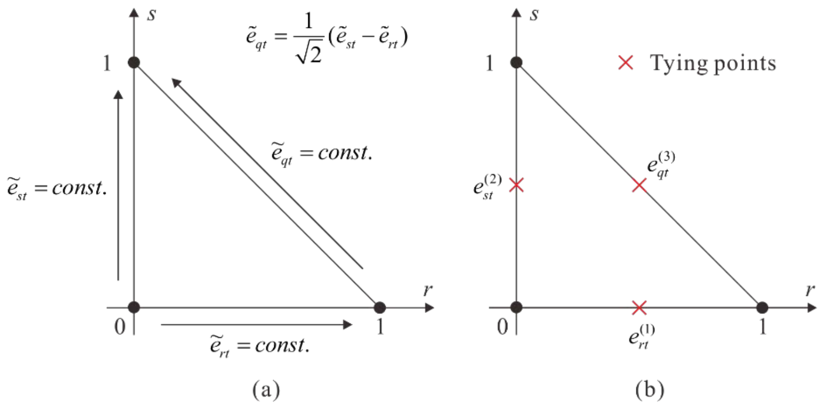

Figure 3.3 (a) The constant covariant transverse shear strain along the edge is shown. (b) The tying points for the assumed shear strain for MITC3 element are given.

However, above a three node triangular shell finite element has some problems in shear locking and it behaves very stiff in bending dominant problems. To reduce this problems, let me introduce the MITC3 element. The MITC3 element has the same interpolation for the geometry and displacement but has a difference when dealing with the transverse shear stress.

The constant covariant transverse shear strain along the edge lines of triangle is assumed to construct shear strain field. The tying points for the assumed shear strain is given as shown in Figure 3.3. The assumed shear strain in covariant component is defined by

$$e_{rt} = e_{rt}^{(1)} + cs, \quad e_{st} = e_{st}^{(2)} - cr, \quad with\ c = e_{st}^{(2)} - e_{rt}^{(1)} - e_{st}^{(3)} + e_{rt}^{(3)}, \tag{3.10}$$

3.2. The velocity potential field

If there is a structure at the boundary surface of fluid domain, the boundary conditions are different and then the final form of the matrix equation is also changed. In the same way like in chapter 2, the fluid domain is considered as irrotational, incompressible, and inviscid fluid. The velocity potential and the normal derivative of the velocity potential will be obtained and it is used to update the shape of a bubble and calculate the boundary conditions for the acceleration potential field.

3.2.1. boundary conditions for the velocity potential

There are both the kinematic boundary conditions and the dynamic boundary conditions in common with the bubble dynamic problems. However, to define the dynamic boundary conditions which mean that the balance of the pressure, we need to know the pressure on the wet surface. Because the hydrodynamic pressure on the wet surface is obtained from the acceleration potential field, we define the boundary conditions except for the dynamic boundary condition for the wet surface in this chapter.

The kinematic boundary condition for the bubble surface is defined from the relation between the velocity of a fluid particle and the velocity potential in the same way in Eqn.(2.11).

$$\mathbf{v} = \nabla\varphi \quad \text{on the bubble surface,} \quad S_b, \tag{3.11}$$

The kinematic boundary condition for the wet surface should satisfy the non-penetration condition. The non-penetration condition means that the velocity of the structure and the velocity of the fluid particle are the same in the normal direction.

$$\frac{\partial\varphi}{\partial n} = \dot{\boldsymbol{u}} \cdot \boldsymbol{n} \quad \text{on the wet surface,} \quad S_w, \tag{3.12}$$

where $\dot{\mathbf{u}}$ is the velocity of the structure point on the wet surface, and $\mathbf{n}$ is the outward normal unit vector.

The dynamic boundary condition for the bubble surface is defined from the balance between the

Bernoulli's equation and the inside pressure in the same way in Eqn.(2.21)

$$\frac{d\varphi}{dt}=\frac{p_{atm}}{\rho}-\frac{p_{g0}}{\rho}\left(\frac{V_0}{V_b}\right)^{\lambda}+\frac{1}{2}\left|\nabla\varphi\right|^2-gz_b \quad \text{on the bubble surface,} \quad S_b\,, \tag{3.13}$$

Form the given velocity potential on the bubble surface and the normal derivative of the potential on the wet surface, we can solve the boundary integral equation [19]. The matrix form for the interaction problem will be studied in next chapter.

3.2.2. Coupled equation for the velocity potential

From the discretizing the boundary surface using the three node triangle element, the matrix form of the integral equation is obtained from Eqn.(2.34).

$$\begin{bmatrix}\mathbf{H}_{bb} & \mathbf{H}_{bs}\\ \mathbf{H}_{sb} & \mathbf{H}_{ss}\end{bmatrix}\begin{bmatrix}\boldsymbol{\varphi}_b\\ \boldsymbol{\varphi}_s\end{bmatrix}=\begin{bmatrix}\mathbf{G}_{bb} & \mathbf{G}_{bs}\\ \mathbf{G}_{sb} & \mathbf{G}_{ss}\end{bmatrix}\begin{bmatrix}\boldsymbol{\varphi}_{n,b}\\ \boldsymbol{\varphi}_{n,s}\end{bmatrix}, \tag{3.14}$$

where the subscripts b and s mean the bubble and the structure, respectively. At a given time, the velocity potential on the bubble surface is known and the normal derivative of the potential on the wet surface can be computed by Eqn.(3.12). Therefore, we need to rearrange the matrix equation in accordance with the unknown variables.

$$\begin{bmatrix}\mathbf{G}_{bb} & -\mathbf{H}_{bs}\\ \mathbf{G}_{sb} & -\mathbf{H}_{ss}\end{bmatrix}\begin{bmatrix}\boldsymbol{\varphi}_{n,b}\\ \boldsymbol{\varphi}_s\end{bmatrix}=\begin{bmatrix}\mathbf{H}_{bb} & -\mathbf{G}_{bs}\\ \mathbf{H}_{sb} & -\mathbf{G}_{ss}\end{bmatrix}\begin{bmatrix}\boldsymbol{\varphi}_b\\ \boldsymbol{\varphi}_{n,s}\end{bmatrix}, \tag{3.15}$$

Solving this equation, we can determine the velocity on the bubble surface using from Eqn.(2.35) to Eqn.(2.38). Although we can update the bubble shape at a given time using the nodal velocity on the bubble surface, we cannot update the wet surface shape which is calculated from the deformation of the structure. To predict the deformation of structure, it will be explained how to compute the hydrodynamic pressure on the wet surface.

3.3. The acceleration potential field

To accurately predict the structural deformation, the hydrodynamic force acting on the wet surface should be calculated precisely [17]. The force can be obtained by integrating the hydrodynamic pressure from the Bernoulli's equation. However, it is difficult to precisely compute the partial derivative of the velocity potential with respect to time. Some research adopted the finite difference method to compute the partial derivative, but it leads numerical instabilities and inaccurate results because the partial derivative using finite difference approximation is not simultaneous value and loose its meaning when the boundary is moving [21]. Therefore, based on the acceleration potential theory, we directly calculate the partial derivative of the velocity potential with respect to time by solving the boundary integral equation one more time [25].

The acceleration of a fluid particle can be defined by

$$\mathbf{a} = \frac{d\mathbf{v}}{dt} = \frac{\partial \mathbf{v}}{\partial t} + \left(\mathbf{v} \cdot \nabla\right)\mathbf{v}, \tag{3.16}$$

where $\mathbf{a}$ and $\mathbf{v}$ are the acceleration and the velocity of a fluid particle. Depending on the definition of the velocity potential, substituting Eqn.(2.11), we can express the acceleration by using the velocity potential.

$$\begin{aligned}\mathbf{a} &= \frac{d\nabla\varphi}{dt} = \frac{\partial \nabla\varphi}{\partial t} + \left(\nabla\varphi \cdot \nabla\right)\nabla\varphi \\ &= \frac{\partial \nabla\varphi}{\partial t} + \nabla\left(\frac{1}{2}\left(\nabla\varphi\right)^2\right) = \nabla\left(\frac{\partial \nabla\varphi}{\partial t} + \frac{1}{2}\left(\nabla\varphi\right)^2\right)\end{aligned}, \tag{3.17}$$

Then, the acceleration of a fluid particle can be obtained by the gradient of the last term in Eqn.(3.17) and, based on the above relation, the nonlinear acceleration potential can be defined as

$$\phi \equiv \frac{\partial \varphi}{\partial t} + \frac{1}{2}\left(\nabla\varphi\right)^2, \tag{3.18}$$

where ϕ and φ is the acceleration potential and the velocity potential, respectively. Similar with the velocity potential whose gradient becomes the velocity, the gradient of the acceleration potential becomes the acceleration. However, in the contrary to the velocity potential that satisfy the Laplace's equation, the acceleration potential doesn't satisfy the equation because the second term of Eqn.(3.18) is nonlinear.

Unlike the acceleration potential, the partial derivative of the velocity potential with respect to time which is the first term of the right hand side of Eqn.(3.18) satisfy the Laplace's equation. Therefore, we solve the boundary integral equation about the φ_t, and the acceleration potential is used for constructing the additional boundary conditions to solve the equation.

3.3.1. Boundary conditions for the acceleration potential

In common with the kinematic boundary condition about the velocity potential on the wet surface, the acceleration potential also should satisfy the non-penetration condition. The kinematic boundary condition for the acceleration potential on the wet surface can be obtained by the scalar product of the outward normal unit vector and the acceleration vector.

$$\frac{\partial \phi}{\partial n} = \ddot{\mathbf{u}} \cdot \mathbf{n} \quad \text{on the wet surface,} \quad S_w, \tag{3.19}$$

where $\ddot{\mathbf{u}}$ is the acceleration vector of the structure at a node. If we take the normal derivative on the both sides of Eqn.(3.18), then the equation can be express as a function of the velocity potential without the acceleration potential.

$$\frac{\partial}{\partial n}\left(\frac{\partial \varphi}{\partial t}\right) + \frac{\partial}{\partial n}\left(\frac{1}{2}(\nabla \varphi)^2\right) = \ddot{\mathbf{u}} \cdot \mathbf{n} \quad \text{on the wet surface,} \quad S_w, \tag{3.20}$$

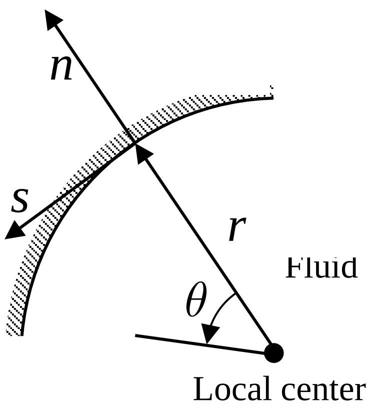

Figure 3.4 In order to calculate the radius directional derivative of the square of the gradient of the potential, the local polar coordinate is introduced. The origin is located at the center of the tangential circle.

The second term of the left side could be calculated in the local polar coordinate whose origin is located on the center of the tangential circle as shown in Figure 3.4 [16]. The radius directional derivative of the square of the gradient of the potential is written as

$$\frac{\partial}{\partial r}\left(\frac{1}{2}(\nabla\varphi)^2\right)=\frac{\partial\varphi}{\partial r}\frac{\partial^2\varphi}{\partial r^2}+\frac{\partial\varphi}{r\partial\theta}\left(-\frac{1}{r}\frac{\partial\varphi}{r\partial\theta}+\frac{1}{r}\frac{\partial^2\varphi}{\partial r\partial\theta}\right), \tag{3.21}$$

where r and θ are the coordinate of the local coordinate system. Also, the Laplace's equation is written as

$$\frac{\partial^2\varphi}{\partial r^2}+\frac{1}{r}\frac{\partial\varphi}{\partial r}+\frac{1}{r^2}\frac{\partial^2\varphi}{\partial\theta^2}=0, \tag{3.22}$$

Substituting Eqn.(3.21) into Eqn.(3.20), the equation is written as

$$\frac{\partial}{\partial r}\left(\frac{1}{2}(\nabla\varphi)^2\right)=-\frac{1}{r}\left\{\left(\frac{\partial\varphi}{\partial r}\right)^2+\left(\frac{\partial\varphi}{r\partial\theta}\right)^2\right\}-\frac{\partial\varphi}{\partial r}\frac{\partial^2\varphi}{r^2\partial\theta^2}+\frac{\partial\varphi}{r\partial\theta}\frac{\partial}{r\partial\theta}\left(\frac{\partial\varphi}{\partial r}\right), \tag{3.23}$$

Furthermore, there are some useful relations.

$$\frac{\partial}{\partial r}\equiv\frac{\partial}{\partial n},\ \frac{\partial}{r\partial\theta}\equiv\frac{\partial}{\partial s},\ \frac{1}{r}\equiv\kappa, \tag{3.24}$$

where κ is the curvature of the tangential circle along the s direction at a node. Using above relations, the final form of the second term of the left side in Eqn.(3.19) can be written as

$$\frac{\partial}{\partial n}\left(\frac{1}{2}(\nabla\varphi)^2\right)=-\kappa\left|\nabla\varphi\right|^2-\frac{\partial\varphi}{\partial n}\frac{\partial^2\varphi}{\partial s^2}+\frac{\partial\varphi}{\partial s}\frac{\partial}{\partial s}\left(\frac{\partial\varphi}{\partial n}\right), \tag{3.25}$$

After solving the velocity potential field, the right side of above equation can be obtained by locally adopting the moving least square using the distributions of the velocity potential and its normal derivative. A local Cartesian is used for calculation and its origin is located at the considered point. The Z direction is same with the normal vector at the node as shown in Figure 3.5. Because we need to obtain the second derivative of the velocity potential, a second order polynomial is used for the interpolation.

$$F(X,Y)=c_1+c_2X+c_3Y+c_4X^2+c_5XY+c_6Y^2, \tag{3.26}$$

where X and Y are the local coordinate of the surrounding nodes.

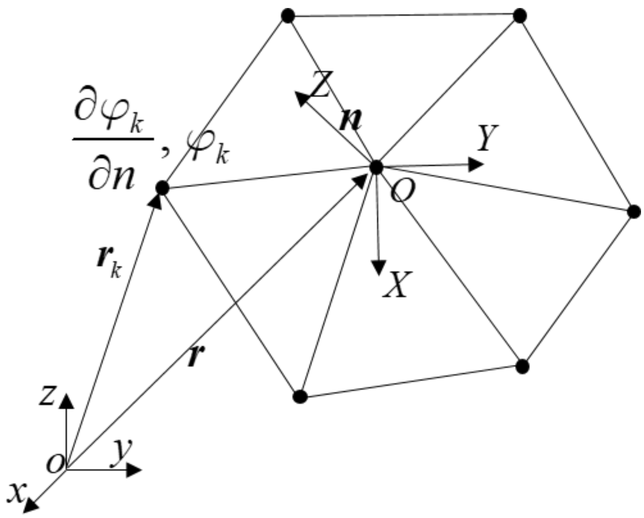

Figure 3.5 The considered node and the surrounding elements and the nodes are shown. The coordinate $o-xyz$ is the global Cartesian coordinate and the coordinate $O-XYZ$ is the local Cartesian whose Z direction is same as the normal vector at the node.

The weight coefficient w_k is defined by using the distance between the considered node and its surrounding nodes. To make the contribution large when the surrounding node is near, the weight w_k is inversely proportional to the exponential function [18].

$$w_k = \exp\left(\frac{-|\mathbf{r}_k - \mathbf{r}|}{2d}\right), \tag{3.27}$$

where $\mathbf{r}_k$ and $\mathbf{r}$ are the position vector of the surrounding nodes and the considered node, respectively. d is the average distance between the surrounding nodes and the considered node.

The coefficients form c_1 to c_6 for the interpolation are determined from the values of the surrounding nodes. Because both the potential field and the normal derivative of the potential field are necessary to compute the Eqn.(3.24), Two error function are defined in accordance with the weighted least square [10].

$$E_1\left(c_1, c_2, c_3, c_4, c_5, c_6\right) = \sum_{k=1}^{N_{surr}} w_k \left[F_1\left(X_k, Y_k\right) - \varphi_k\right], \tag{3.28}$$

$$E_2\left(c_1,c_2,c_3,c_4,c_5,c_6\right)=\sum_{k=1}^{N_{surr}} w_k\left[F_2\left(X_k,Y_k\right)-\left(\frac{\partial\varphi}{\partial n}\right)_k\right], \qquad (3.29)$$

where E_1 and E_2 are the error function for the surface interpolation for the velocity potential and for the normal derivative of the velocity potential, respectively. N_{surr} is the number of the surrounding nodes.

The coefficients, c_j, are obtained by minimizing the error function. In order to make the error function minimized, the derivatives of error function with respect to the coefficients should be zero.

$$\frac{\partial E\left(c_1,c_2,c_3,c_4,c_5,c_6\right)}{\partial c_j}=0, \quad \text{for j = 1, 2, …, 6.} \qquad (3.30)$$

Substituting from Eqn.(3.25) to Eqn.(3.28) into Eqn.(3.29), the matrix form the equation is obtained by

$$\sum_{j=1}^{6} A_{ij}c_j = B_j^n, \text{ for i = 1, 2, …, 6,} \qquad (3.31)$$

where $\mathbf{A}$ and $\mathbf{B}$ are made up of the local position, the weight, and the value at the surrounding nodes including the considered node. $\mathbf{B}^1$ and $\mathbf{B}^2$ are for the E_1 and E_2, respectively.

$$A_{ij}=\sum_{k=1}^{N_{surr}} w_k\beta_{ki}\beta_{kj}, \qquad (3.32)$$

$$B_i^1=\sum_{k=1}^{N_{surr}} w_k\beta_{ki}\varphi_k, \qquad (3.33)$$

$$B_i^2=\sum_{k=1}^{N_{surr}} w_k\beta_{ki}\left(\frac{\partial\varphi}{\partial n}\right)_k, \qquad (3.34)$$

The β_{ki} value is determined as below.

$$\begin{aligned}&\beta_{k1}=1, \quad \beta_{k2}=X_k, \quad \beta_{k3}=Y_k,\\ &\beta_{k4}=X_k^2, \quad \beta_{k5}=X_kY_k, \quad \beta_{k6}=Y_k^2, \text{ for k = 1, 2, …, } N_{surr}.\end{aligned} \qquad (3.35)$$

After determining the coefficients for the interpolation for the normal derivative of the velocity potential, and the velocity potential, the normal derivative of the square of the gradient of the velocity potential is easily obtained. In this study, since the finite shell element is only formulated for the linear elastic range, the displacement is small enough. Therefore, the curvature of the tangential circle is negligible and assumed as zero.

The right side term in Eqn.(3.19) could be calculated from the structural governing equation.

$$\mathbf{N}\ddot{\vec{U}} = \mathbf{N}\mathbf{M}^{-1}\left(\vec{R} - \mathbf{K}\vec{U}\right), \tag{3.36}$$

where $\mathbf{M}$, $\mathbf{K}$, $\vec{U}$, $\ddot{\vec{U}}$, and $\vec{R}$ are the mass matrix, the stiffness matrix, the nodal displacement vector, the nodal acceleration vector, and the external force vector, respectively. the external force can be obtained by integrating the hydrodynamic pressure from the unsteady Bernoulli equation.

$$\vec{R} = -\rho_w\left[\sum_m \int_{S_m} \mathbf{H}^T \mathbf{n} dS\right]\vec{\varphi}_t - \rho_w\left[\sum_m \int_{S_m} \mathbf{H}^T \frac{\left|\nabla\varphi\right|^2}{2} \mathbf{n} dS\right], \tag{3.37}$$

Let us define a coefficient matrix $\mathbf{C}$ and an array for the values of Eqn.(3.24) at each node to express the Eqn.(3.19) simply,

$$\mathbf{C} \equiv \rho_w \mathbf{N}\mathbf{M}^{-1}\left[\sum_m \int_{S_m} \mathbf{H}^T \mathbf{n} dS\right], \quad \mathbf{T} \equiv \begin{bmatrix} \left|\nabla\varphi\right|_1^2 \\ \vdots \\ \left|\nabla\varphi\right|_{N_s}^2 \end{bmatrix}, \tag{3.38}$$

Substituting Eqn.(3.25) into Eqn.(3.19), the final form of the matrix equation is obtained by

$$\boldsymbol{\varphi}_{tn} + \mathbf{C}\boldsymbol{\varphi}_t = -\frac{1}{2}\mathbf{C}\mathbf{T} - \mathbf{N}\mathbf{M}^{-1}\mathbf{K}\vec{U} + \frac{\partial}{\partial n}\mathbf{T}\text{, on the wet surface, } S_w. \tag{3.39}$$

The matrix C, M, K, and N are calculated only from the geometry and the properties of the structure and the array T can be obtained by solving the velocity potential field, and the nodal displacement U is initially given.

Therefore, the right side of above equation is all known values and denoted by beta.

$$\boldsymbol{\varphi}_{tn} + \mathbf{C}\boldsymbol{\varphi}_t = \boldsymbol{\beta} \text{ on the wet surface, } S_w. \tag{3.40}$$

The kinematic boundary condition for the acceleration potential has changed into the additional boundary condition for the velocity potential. This additional condition will be used for directly solving the boundary integral equation to obtaining the time derivative of the velocity potential.

3.3.2. Coupled equation for the acceleration potential

For the numerical calculation of the interaction between the underwater explosive bubble and the floating structure, the hydrodynamic force acting on the structure surface should be accurately calculated. The loads acting on the structure are obtained by integrating the hydro dynamic pressure over the surface and the unsteady Bernoulli equation is used to obtain the hydro dynamic pressure. However, the main difficulty is on the calculation of partial derivative of the velocity potential which is one of the terms of the Bernoulli equation.

As mentioned in introduction, the finite difference approximation is widely used for the calculation of the partial derivative of the velocity potential, because it is easy to implement with a little effort. However, the approximated value often causes the numerical instability because it is not instantaneous value. Moreover, when considering the interaction problems which have the movable and deformable boundary, the finite difference approximation is not suitable, because the position of the nodes is also changed. In this case, the meaning of the approximated value obtaining from the finite difference method is much closer to the material derivatives rather than the partial derivatives with respect to the time. There are some efforts to make correction by using the relation between the material derivatives and the partial derivative. However, there is still inaccurate when the time step is very small in the initial and the final stage of the bubble pulsation

In order to obtain the hydro dynamic pressure accurately and stably, the direct calculation methods to get the partial derivative of the velocity potential with respect time are studied recently. In this study, to construct the fully coupled model, the nonlinear acceleration potential is introduced and its non-penetration condition at the boundary surface is used. To directly calculate the time derivative, the boundary integral equation for the time derivative of the velocity potential is solved because it satisfies the Laplace equation also.

$$C(P)\varphi_t(P) = \int_S \left(G(P,Q)\frac{\partial \varphi_t(Q)}{\partial n} - \varphi_t(Q)\frac{\partial G(P,Q)}{\partial n} \right) dS, \tag{3.41}$$

where the subscript t means the partial derivative with respect to time. The above equation is derived in the same way in chapter 2.1. The matrix form is expressed as below

$$\begin{bmatrix} \mathbf{H}_{bb} & \mathbf{H}_{bs} \\ \mathbf{H}_{sb} & \mathbf{H}_{ss} \end{bmatrix} \begin{bmatrix} \boldsymbol{\varphi}_{t,b} \\ \boldsymbol{\varphi}_{t,s} \end{bmatrix} = \begin{bmatrix} \mathbf{G}_{bb} & \mathbf{G}_{bs} \\ \mathbf{G}_{sb} & \mathbf{G}_{ss} \end{bmatrix} \begin{bmatrix} \boldsymbol{\varphi}_{tn,b} \\ \boldsymbol{\varphi}_{tn,s} \end{bmatrix}, \tag{3.42}$$

where the subscript n means the partial derivative with respect to the normal direction [21].

Depending on the relation between the gas pressure inside the explosive bubble and the Bernoulli equation, the time derivative of the velocity potential can be determined similarly with Eqn.(2.18)

$$\frac{\partial \varphi}{\partial t} = \frac{p_{atm}}{\rho} - \frac{p_{g0}}{\rho} \left(\frac{V_0}{V_b} \right)^{\lambda} - \frac{1}{2} \left| \nabla \varphi \right|^2 - g z_b \text{, on the bubble surface, } S_b . \tag{3.43}$$

Rearrange the Eqn.(3.42) for the unknowns,

$$\begin{bmatrix} \mathbf{G}_{bb} & -\mathbf{H}_{bs} & \mathbf{G}_{bs} \\ \mathbf{G}_{sb} & -\mathbf{H}_{ss} & \mathbf{G}_{ss} \end{bmatrix} \begin{bmatrix} \boldsymbol{\varphi}_{tn,b} \\ \boldsymbol{\varphi}_{t,s} \\ \boldsymbol{\varphi}_{tn,s} \end{bmatrix} = \begin{bmatrix} \mathbf{H}_{bb} \boldsymbol{\varphi}_{t,b} \\ \mathbf{H}_{sb} \boldsymbol{\varphi}_{t,b} \end{bmatrix}, \tag{3.44}$$

The number of unknowns is $N_b + 2N_s$ and the number or equations is $N_b + N_s$. Therefore, the above equation is underdetermined. To solve this equation, we need more conditions and the condition is obtained from the non-penetration condition for the acceleration condition in chapter 3.3.3. The matrix form of the additional boundary condition is in Eqn.(3.39).

Substituting Eqn.(3.40) in Eqn.(3.44) yields

$$\begin{bmatrix} \mathbf{G}_{bb} & -\mathbf{H}_{bs} & \mathbf{G}_{bs} \\ \mathbf{G}_{sb} & -\mathbf{H}_{ss} & \mathbf{G}_{ss} \\ 0 & \mathbf{C} & \mathbf{I} \end{bmatrix} \begin{bmatrix} \boldsymbol{\varphi}_{tn,b} \\ \boldsymbol{\varphi}_{t,s} \\ \boldsymbol{\varphi}_{tn,s} \end{bmatrix} = \begin{bmatrix} \mathbf{H}_{bb} \boldsymbol{\varphi}_{t,b} \\ \mathbf{H}_{sb} \boldsymbol{\varphi}_{t,b} \\ \boldsymbol{\beta} \end{bmatrix}, \tag{3.45}$$

Solving the above equation, the time derivative of the velocity potential is directly calculated and then, the hydro dynamic pressure can be obtained simultaneously and instantaneously considering both the response of the structure and the bubble dynamics. Because we consider the response of the structure in the coupled model, there is no need to compute the added mass effect.

3.4. Results

After validating the implemented code both of the bubble dynamics using the boundary element method and the shell element using the finite element method, respectively, the coupled model for the interaction between the bubble and the structure is studied. To validate presented model, we make comparisons between the results of the coupled model and the results of the bubble dynamics under the two extreme structural stiffness. Additionally, a circular steel plate case is studied for the numerical example and it is compared with the commercial tool(LS-DYNA). Finally, the behavior of the bubble over the various stiffness of the plate was studied.

Figure 3.6 shows the computational domain considered. For the simplicity of the numerical simulation, the radius of the floating plate is set to ten times larger than the maximum radius of the explosive bubble and the outer most nodes of the floating plate are fixed, so it is enough to neglect the effect of the free surface outside the plate[]. All the numerical simulations in this chapter have the same conditions in the weight of the TNT, the initial depth of the explosion, and the radius of the floating plate as shown in Table 3.1. The potential is initially zero.

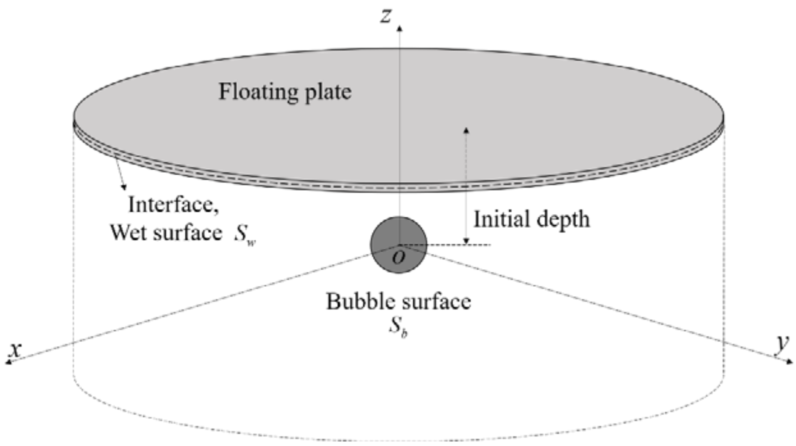

Figure 3.6 The solution domain and the schematic configuration for the interaction between an underwater explosive bubble and a floating plate.

Table 3.1 Parameters for bubble and the radius of the plate

Structure parameters		
TNT	5	(g)
Initial depth	0.25	(m)
Radius of the plate	2.6	(m)

3.4.1. Comparison between the high stiffness wall and the rigid wall

When the structure has high stiffness with infinitely large Young's modulus and extremely small Poisson ratio, the structural behavior is close to the rigid body and then the structure can be regarded as the rigid body. The properties of the structure are shown in Table 3.2. Figure 3.7 and 3.8 shows the behavior of the bubble and the response of the structure in the expansion stage of the bubble.

(a)

(b)

(c)

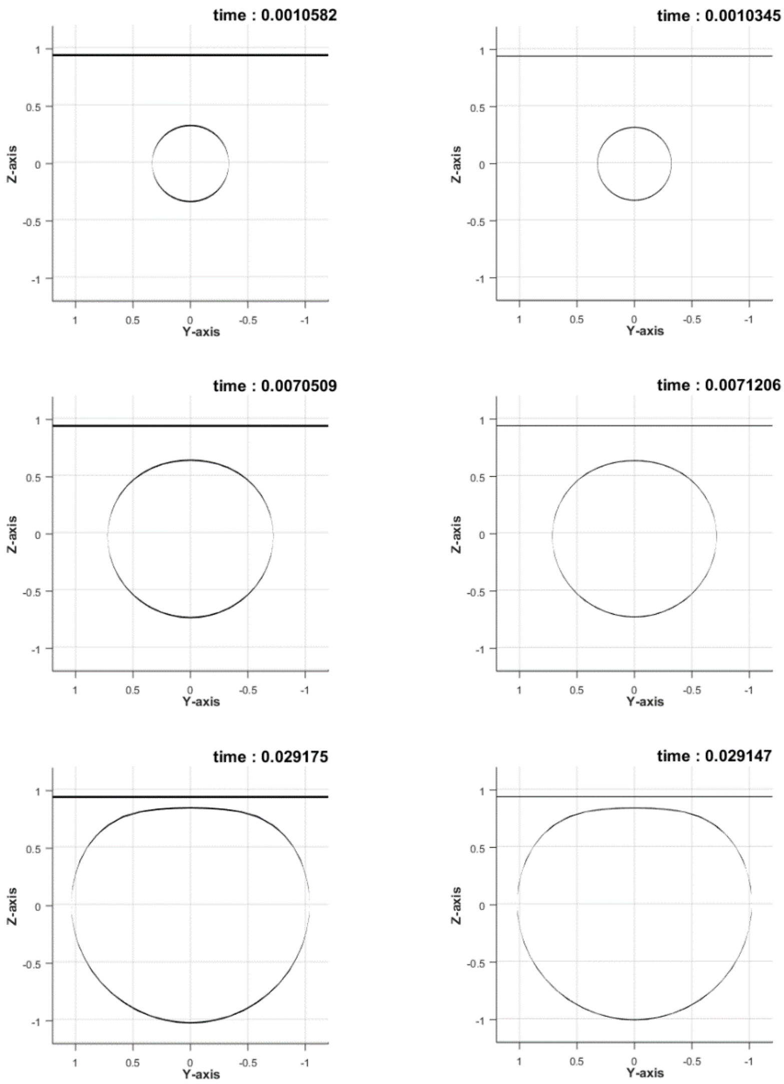

Figure 3.7 The result of the high stiffness wall and the rigid wall case in expansion stage. The left side is the coupled model for interaction and the right side is the bubble dynamics under the ideal rigid wall.

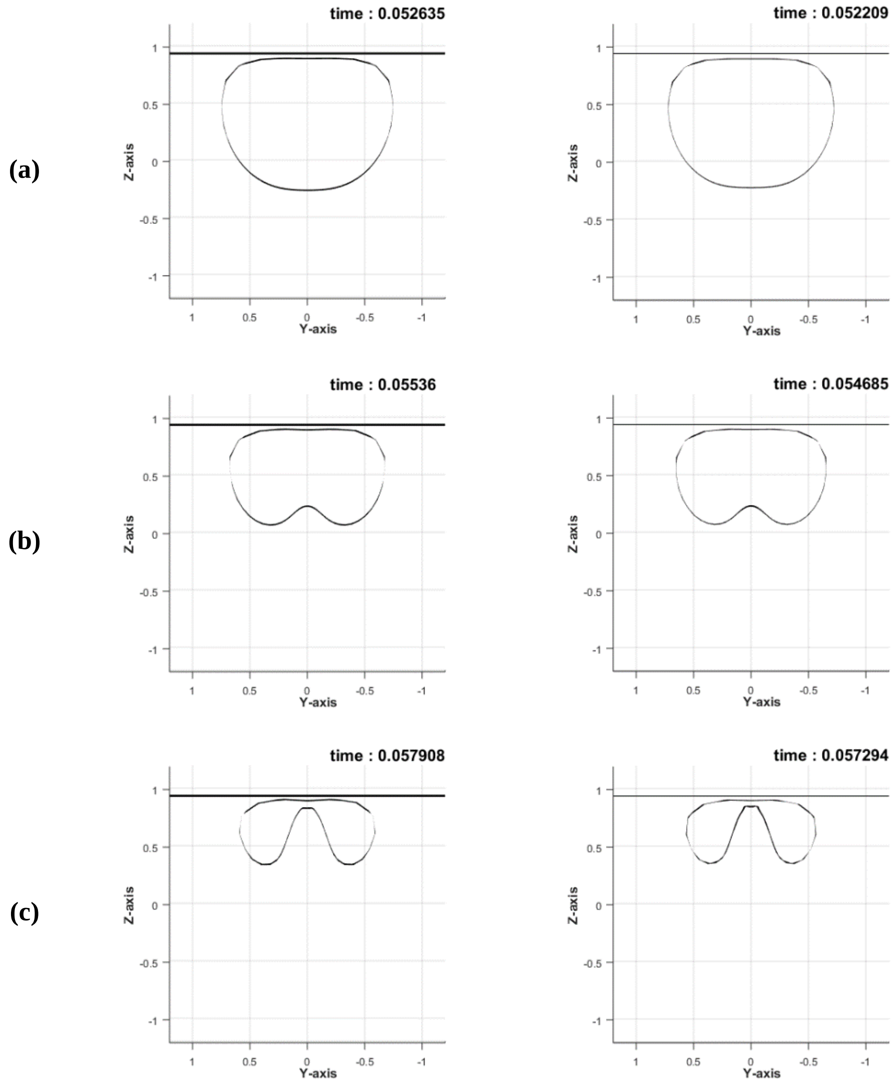

Figure 3.8 The result of the high stiffness wall and the rigid wall case in collapse stage. The left side is the coupled model for interaction and the right side is the bubble dynamics under the ideal rigid wall.

In the early stage of the expansion, Figure 3.7 (a), the bubble maintains the spherical shape because of the high internal gas pressure of the bubble. Soon after, the bubble loses its spherical shape and the top surface of the bubble becomes flattened along the wet surface. When the bubble reaches its maximum volume, Figure 3.7 (c), the bubble is elongated in the normal direction of the wet surface. Then, the bubble starts to collapse. Figure 3.8 shows that the response of the structure and the behavior of the bubble in the collapse stage of the bubble. The bottom surface of the bubble is attracted toward the structure as shown in Figure 3.8 (b). Finally, it develops the strong jet flow as shown in Figure 3.8 (c).

Table 3.2 Structure parameters for high stiffness plate case

Structure parameters		
Young's modulus (E)	2.1e14	(N/m^2)
Poisson ratio (υ)	0	-
Density (ρ_s)	7800	(kg/m^3)
Thickness (t)	0.1	(m)

The overall behavior of the bubble under the high stiffness plate is well matched with the bubble dynamics result under the rigid wall case. Additionally, during the whole simulation, the displacement of the plate is small enough to be neglected. Figure 3.9 shows that the volume of the bubble and the z-directional displacement at the center over time, respectively. The maximum volume of the bubble is close to $0.08m^3$ and the period is about 0.058sec in both cases. The displacement at the center of the plate is close to zero.

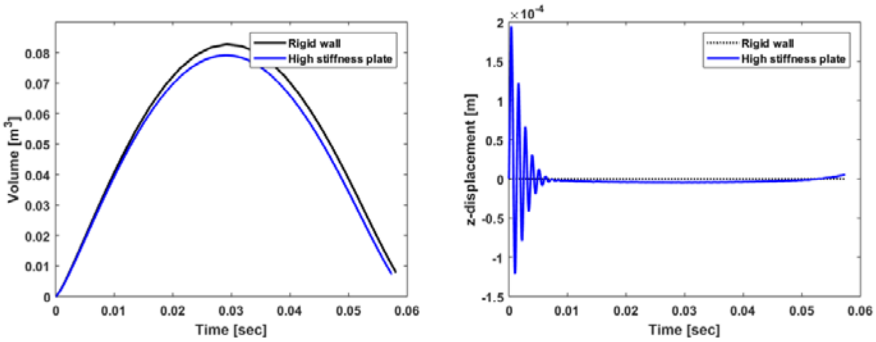

Figure 3.9 The volume of the bubble and the z-directional displacement at the center of the plate over time are shown. The blue line is for the interaction model coupled with high stiffness wall and the black line is for the bubble dynamics under the rigid wall.

3.4.2. Comparison between the low stiffness plate and the free surface

When the structure has low stiffness with extremely small Young's modulus and Poisson ratio tends to 0.5, the structural behavior is close to the free surface and then the structure can be regarded as non-existence. The properties of the structure are shown in Table 3.3. Figure 3.10 shows the behavior of the bubble and the response of the structure in the expansion stage of the bubble. During the simulation, the overall behaviors of the bubble are well matched and the deformed shapes of the plate and the free surface are also in agreement with each other.

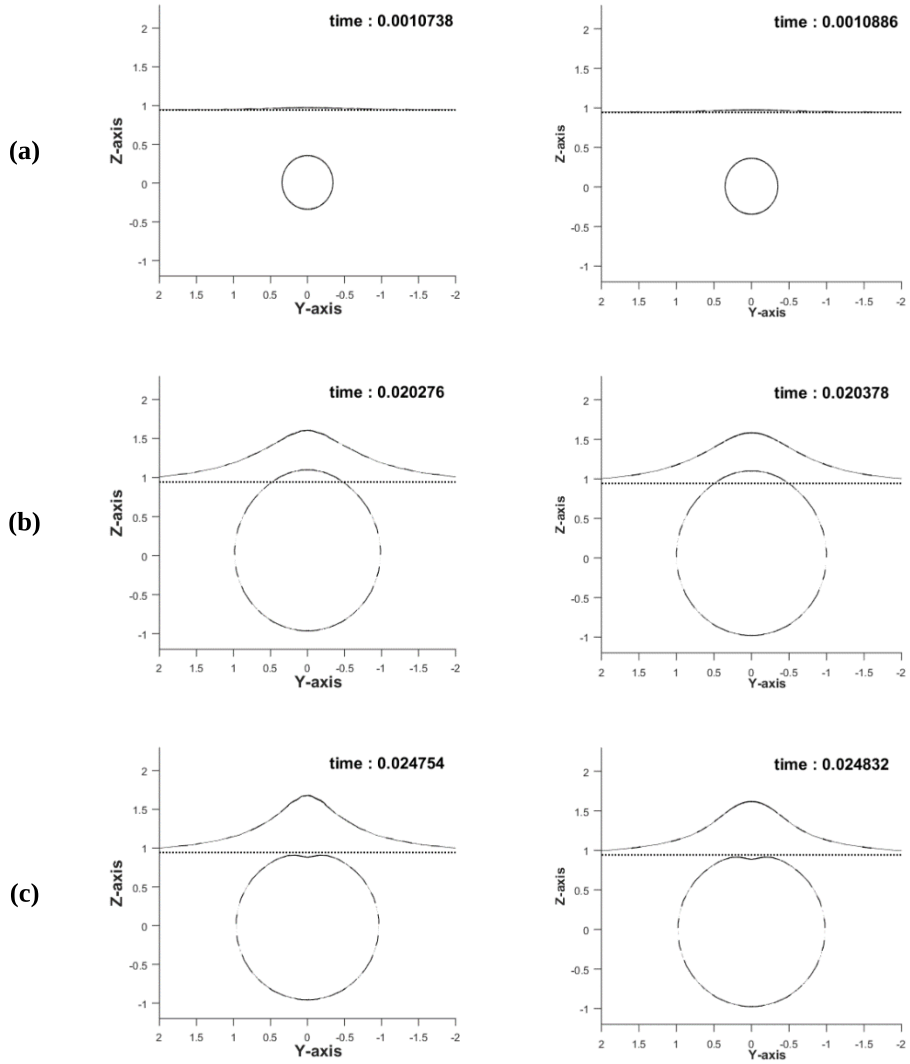

Figure 3.10 The result of the low stiffness wall and the free surface case in expansion stage. The left side is the bubble dynamics under the free surface and the right side is the proposed coupled model for interaction.

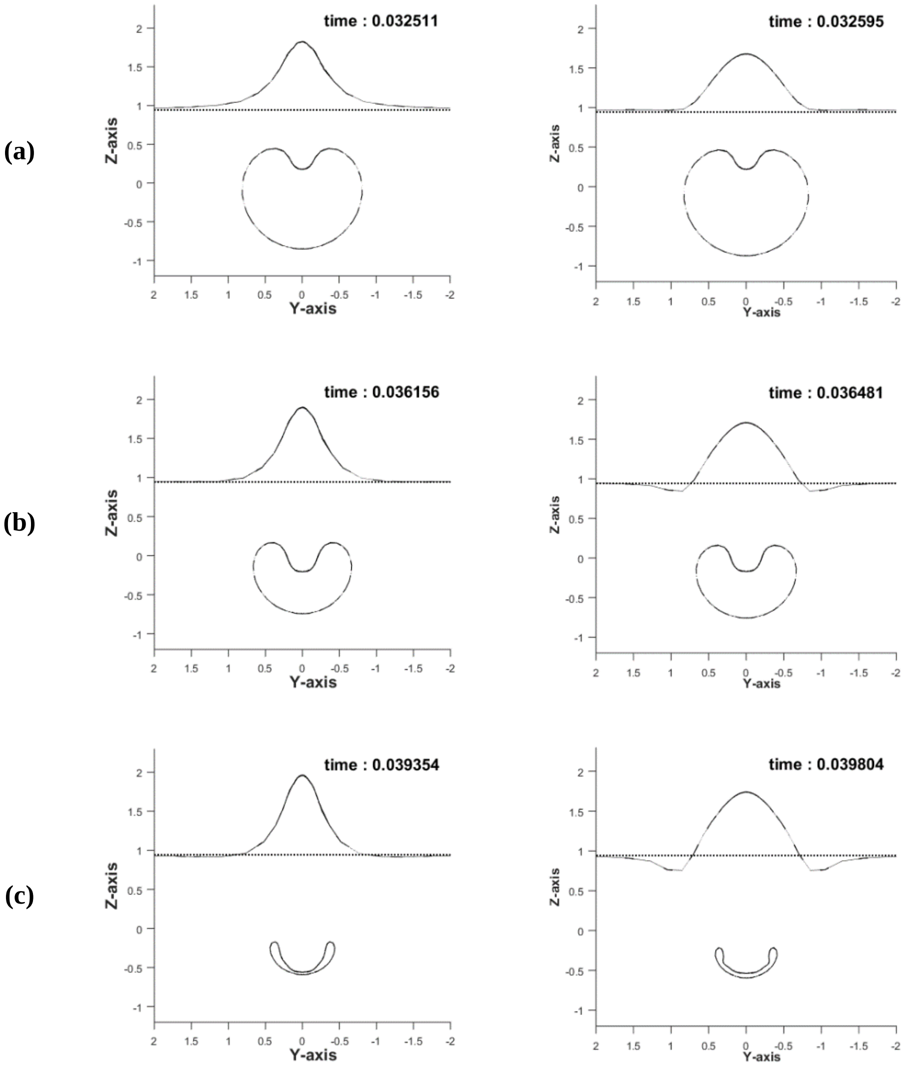

Figure 3.11 The result of the low stiffness wall and the free surface case in collapse stage. The left side is the bubble dynamics under the free surface and the right side is the proposed coupled model for interaction.

As shown in the Figure 3.10 (a), the bubble maintains the spherical shape right after detonation for a little because of the high internal gas pressure of the bubble and the wet surface is slightly swollen. Then, the bubble loses its spherical shape and is elongated along the z direction at the top and bottom surface both. When the bubble reaches its maximum volume, Figure 3.10 (b), the top surface of the bubble is positioned above the base free surface at this moment. The bubble starts to collapse after reaching its maximum volume as shown in Figure 3.11. The top surface is moved toward the bottom surface and the jet flow is developed along the movement of the bubble surface.

Table 3.3 Structure parameters for low stiffness plate case

Structure parameters		
Young's modulus (E)	2.0e5	(N/m^2)
Poisson ratio (υ)	0.48	-
Density (ρ_s)	1700	(kg/m^3)
Thickness (t)	0.001	(m)

The overall behavior of the bubble under the low stiffness plate is well matched with the bubble dynamics result under the free surface case. Additionally, during the expansion stage, the deformed shape of the plate is also well matched with the shape of the free surface but during the collapse stage, the deformed shape of the plate is slightly different with the shape of the free surface because the stiffness of the structure is small, but still exists. Figure 3.12 shows that the volume of the bubble and the z-directional displacement at the center of the plate over time, respectively. The maximum volume of the bubble is about 0.08m^3 and the period is about 0.04sec in both cases.

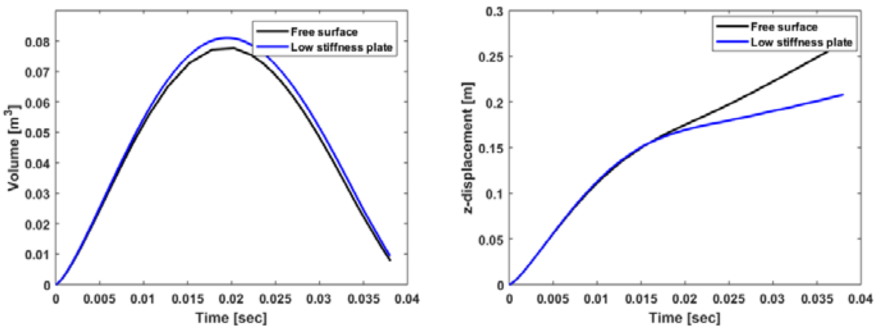

Figure 3.12 The volume of the bubble and the z-directional displacement at the center of the plate over time are shown. The blue line is for the interaction model coupled with low stiffness wall and the black line is for the bubble dynamics under the free surface.

3.4.3. Numerical example for steel plate

In this section, the hydroelasic response of floating plate structure is studied and the results are compared with the commercial tool(LS-DYNA). The properties of the structure are shown in Table 3.4. The plate model, the position of the detonation and the weight of TNT in chapter 3.4 are used again. Figure3.13 shows the behavior of the bubble and the response of the structure in the expansion stage of the bubble. The behavior of the bubble and the displacement of the plate are compared at each time.

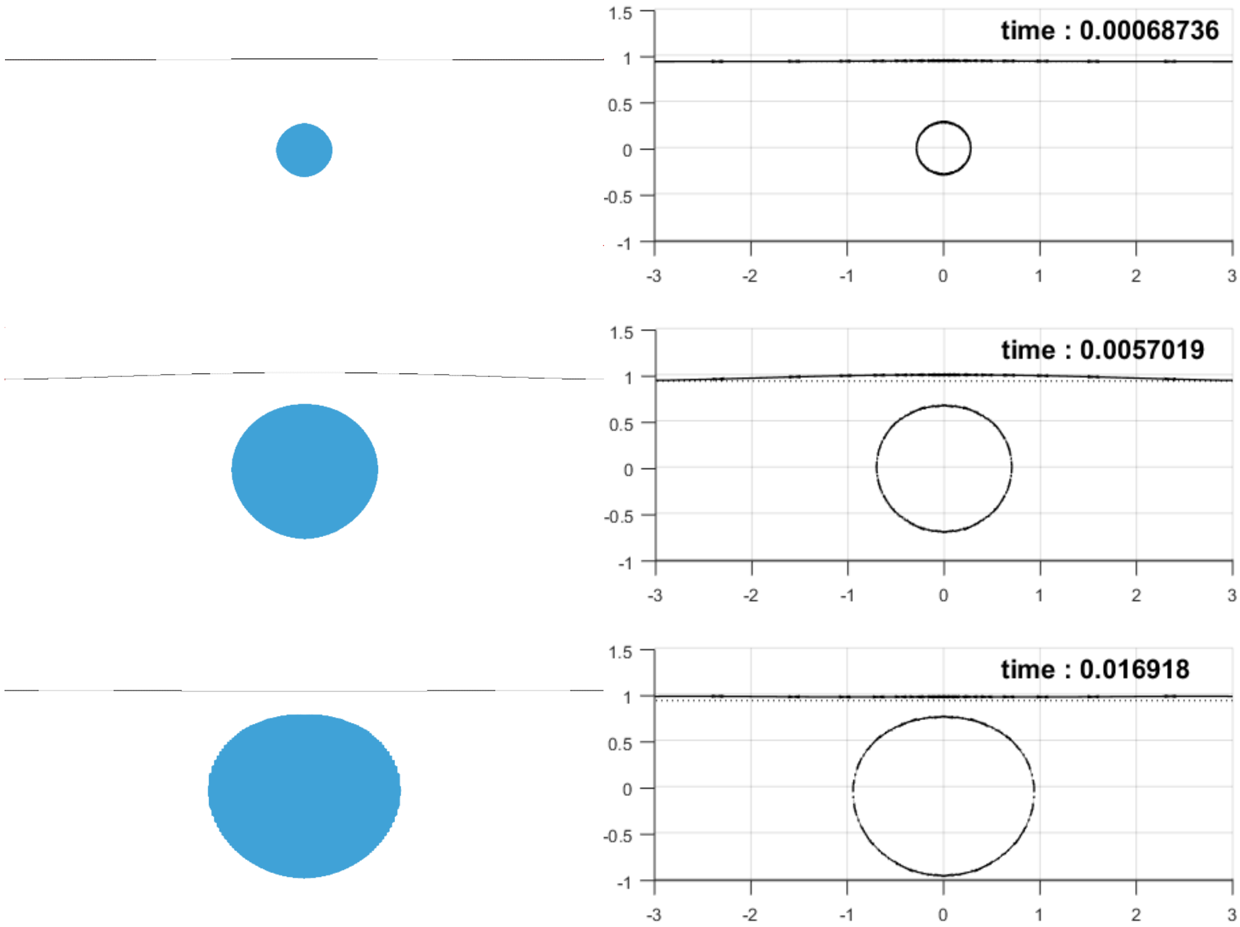

Figure 3.13 The response of the steel plate and the behavior of the explosive bubble in expansion stage are shown. The left side is the result of the LS-DYNA and the right side is the result of the implemented code.

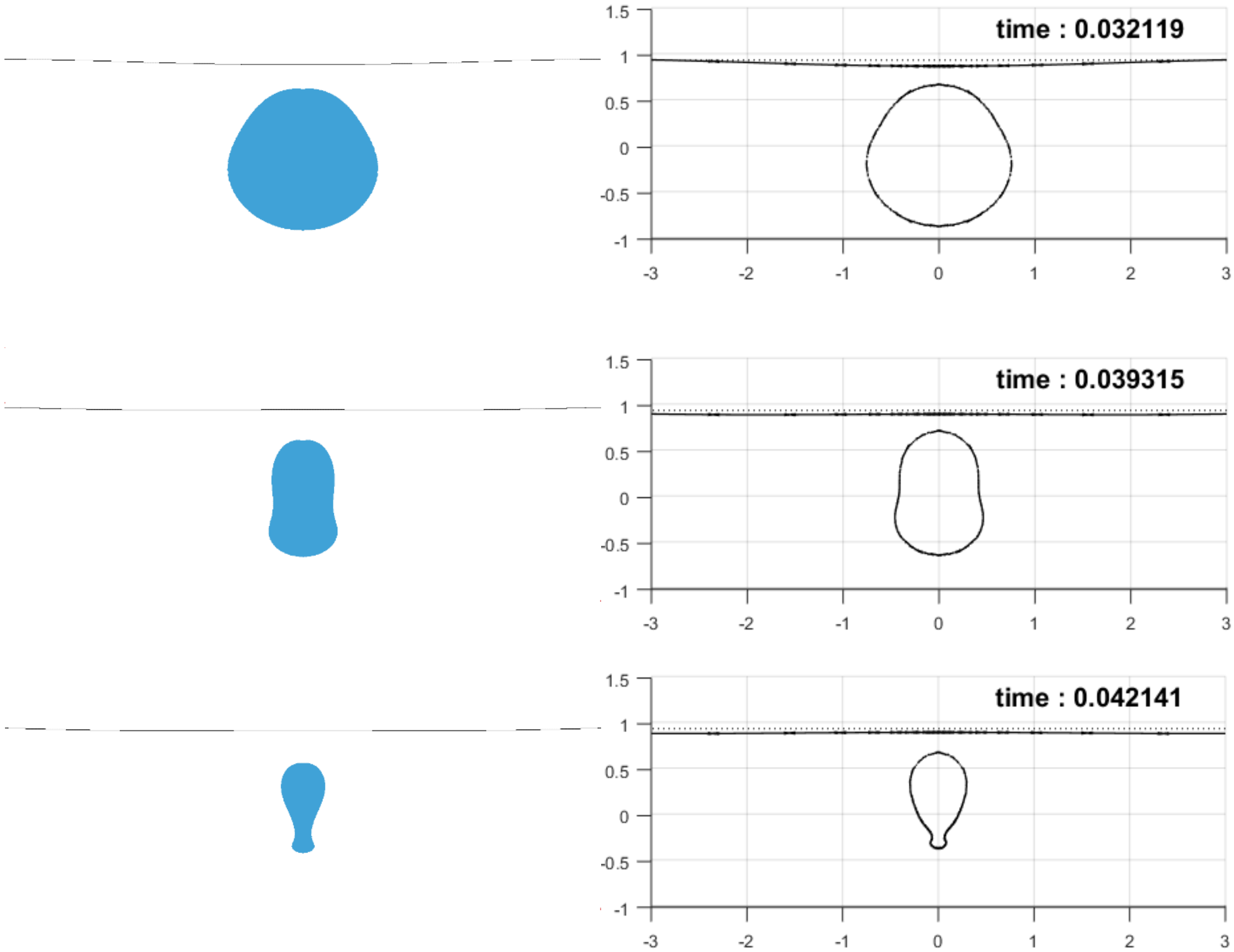

Figure 3.14 The response of the steel plate and the behavior of the explosive bubble in collapse stage are shown. The left side is the result of the LS-DYNA and the right side is the result of the implemented code.

As shown in the Figure 3.13 (a), the bubble keeps its initial spherical shape at the beginning and then, the bubble violently grows up losing its spherical shape while deforming above plate. The maximum displacement at the center occurs before the bubble reaches its maximum volume as shown in Figure 3.13(b). Afterwards, the plate is attracted and moves downwards while the bubble still expands. Because of the influence of the floating plate, the top surface of the bubble moves slower than the bottom surface, which makes bubble elongated in direction normal to the wet surface. Moreover, the bubble does not expand sufficiently in volume as shown in Figure 3.13 (c).

Table 3.4 Structure parameters for numerical example

Structure parameters		
Young's modulus (E)	2.03e11	(N/m^2)
Poisson ratio (υ)	0.3	
Density (ρ_s)	7800	(kg/m^3)
Thickness (t)	0.01	(m)

Due to the influence of the deformable moving boundary, the volume of the bubble and its period are significantly changed. The maximum volume of the bubble decrease to $0.06m^3$ and also the period decrease to $0.04\mathrm{sec}$ compared with the results in chapter 3.4.1. Figure 3.15 shows that the volume of the bubble and the z-directional displacement at the center of the plate over time, respectively. The deformation of the floating plate and the overall behaviors of the bubble are in general agreement in both results from the implemented code and the commercial tool. There are some differences in the maximum displacement and its occurrence time in Table 3.5 because the different numerical methods and the finite element are used.

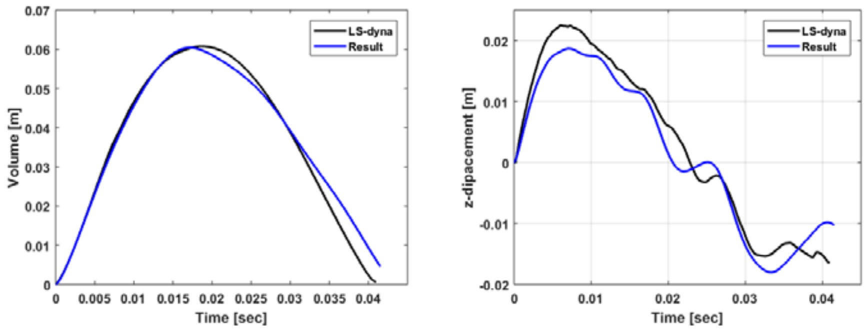

Figure 3.15 The volume of the bubble and the z-directional displacement at the center of the plate over time are shown. The results of the implanted codes are blue line and the result of the LS-DYNA are black line.

Table 3.5 Maximum values of the results in the Figure 3.15

	Maximum volume	Period	Maximum displacement	Occurrence time
LS-DYNA	6.075e-2	4.044e-2	2.249e-2	6.001e-3
Implemented code	6.041e-2	4.212e-2	1.871e-2	7.126e-3

3.4.4. The behavior of the bubble depending on the rigidity of the plate

The maximum volume of the bubble, the period, and the final bubble shape are studied in this chapter because the boundary surface has a significant effect on the behavior of the bubble [24]. The geometric information and the initial parameters in Figure 3.6 and Table 3.1 used again. The flexural rigidity of the plate is expressed as

$$D = \frac{Et^3}{12\left(1-\nu^2\right)}, \qquad (3.46)$$

where E, v, and t are the Young's modulus, Poisson ratio, and the thickness of the plate.

Figure 3.15 shows that the maximum volume and the period depending on the various flexural rigidity of the plate in logarithmic scale. The closer to the left is flexible and the closer to the right is stiff. As mentioned in chapter 3.4.1 and 3.4.2, the plate can be regarded as a rigid wall or the free surface when the stiffness of the plate is extremely large or small. There is a transient section between 4 and 8 as shown in Figure 3.15. In that range, the period becomes larger from 0.04 sec to 0.06 sec as the rigidity increases. However, the maximum volume decreases from $0.08m^3$ to $0.06m^3$ which is its minimum, and then, increases to $0.08m^3$ again. Additionally, the direction of jet flow is changed from downward to upward, and the occurrence location is changed from upper surface to lower surface of the bubble as the rigidity of the plate increases.

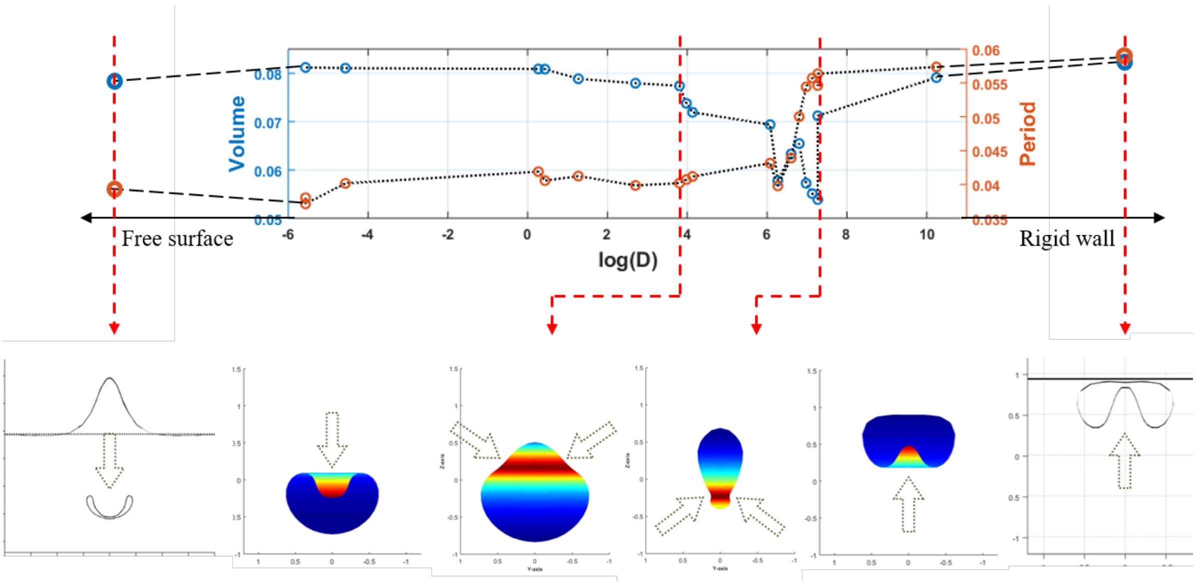

Figure 3.16 The behavior of the bubble depending on the rigidity of the plate.

Chapter 4. Conclusion

In this study, the fully coupled model between the bubble dynamics and the floating structure is constructed. For the bubble dynamics, the fluid is modeled by using the boundary element method with the assumption of ideal fluid which is irrotational, inviscid, and incompressible. For the structural domain, the floating structure is modeled with MITC3 shell element by using the finite element method.

Contrary to the most previous study using the finite difference approximation to obtain the partial derivative of the velocity potential, the derivative is directly calculated by solving one more boundary integral equation. To solve the underdetermined problems at this approach, the additional equations can be constructed by defining the nonlinear acceleration potential. Based on the boundary conditions for the acceleration potential, we can construct the fully coupled model instantaneously and simultaneously considering both the response of the structure and the bubble dynamics.

When constructing the additional equation for the coupled model, some derivatives of the potential and its normal derivative should be computed, which are extremely complex. In this study, to avoid the complexity, we apply the surface fitting for the potential field and its normal derivative field, respectively. The second order equation is used for the interpolation and to make the error minimized, the weighted least square method is used. The weight is determined in accordance with the distance from the considered node. The complex computation for calculating the coupled equation terms could be avoided by using some interpolation coefficients.

Prior to constructing the couple model, the bubble dynamics and finite element analysis using MITC3 are validated, respectively. The underwater explosion near a rigid wall is compared with the previous study and the underwater explosion near a free surface is compared with the experimental result. In each case, the period and the maximum volume are well matched and the behavior of the bubble is also matched with the result. The finite element analysis is validated by using the commercial tool, ADINA. The individual results are used to validate the implemented coupled model in two extreme cases.

If the stiffness of the floating plate is very large, the plate can be regarded as rigid wall. Therefore, the interaction between a bubble dynamics and the high stiffness wall is compared with the underwater explosion near a rigid wall. Because of the large stiffness, the displacement of the plate is small enough to neglect. The volume of the bubble and the period is close to the rigid wall case, and the behavior of the bubble is also well matched over time. If the stiffness of the floating plate is very small, the plate can be regarded as non-existence. Therefore, the interaction between a bubble dynamics and the low stiffness wall is compared with the underwater explosion near a free surface. The volume of the bubble and the period is close to the free surface case, and the behavior of the bubble is similar over time as well. However, the z directional displacement at the center node is a bit different because the stiffness of the structure is small, but it still exists. From this comparison with two extreme case, the implemented code is indirectly validated.

For the numerical example, the steel circular plate is simulated and the result is compared with the commercial tool, LS-DYNA. The overall behavior of the bubble, the period, and the volume are close to each other and the displacement at the center node is compared. The maximum displacement and the minimum displacement occur almost similarly, but the magnitude is different because the different numerical method and the finite element are used for each.

Interaction between the bubble dynamics and the structure is studied and the fully coupled model is implemented in three dimension for the expandability of an arbitrary shape of structure. the response of the floating structure and the bubble dynamics is studied over the stiffness of the plate. Under the same weight of TNT and the initial depth, the period of the bubble and the volume is increased as the stiffness is increased. In this study, the bubble dynamics can only simulate right before the jet impact occur, and the structural dynamics is for linear elastic range. Therefore, the toroidal bubble model would be added and the plasticity or the geometrical nonlinear would also considered.

Bibliography

[1] B. B. Taib, “Boundary integral method applied to cavitation bubble dynamics,” Doctor of Philosophy, Department of Mathematics, University of Wollongong, (1985)

[2] Q. X. Wang, K. S. Yeo, B.C. Khoo, K. Y. Lam “Nonlinear interaction between gas bubble and free surface,” Computers and Fluids, 25, 607-628, (1996)

[3] Q. X. Wang, “The Evolution of a Gas Bubble Near an Inclined Wall,” Theoret. Comput. Fluid Dynamics, 12, 29-51, (1998)

[4] Y. L. Zhang, K. S. Yeo, B. C. Khoo, W. K. Chong, “Three-Dimensional Computation of Bubbles Near a Free Surface,” Journal of Computational Physics, 146, 105-123, (1998)

[5] Y. L. Zhang, K. S. Yeo, B. C. Khoo, C. Wang, “3D Jet Impact and Toroidal Bubbles,” Journal of Computational Physics, 166, 336-360, (2001)

[6] P. J. Harris, “An investigation into the use of the boundary integral method to model the motion of a single gas or vapour bubble in a liquid,” Engineering Analysis with Boundary Elements, 28, 325-332, (2004)

[7] E. Klaseboer, B. C. Khoo, K. C. Hung, “Dynamics of an oscillating bubble near a floating structure,” Journal of Fluids and Structures 21, 395-412, (2005)

[8] E. Klaseboer, K. C. Hung, B.C. Khoo, H. Charlier, “Experimental and numerical investigation of the dynamics of an underwater explosion bubble near a resilientrigid structure,” Journal of Fluid Mech., 537, 387-413, (2005)

[9] N. Zhang, Z. Zong, “Hydro-elastic-plastic dynamic response of a ship hull girder subjected to an underwater bubble,” Journal of Marine Structures, 29, 177-197, (2012)

[10] K. M. Manmi, “Three dimensional acoustic microbubble dynamics near rigid boundary,” Doctor of Philosophy, Department of Mathematics, University of Birmingham, (2015)

[11] Y. L. Liu, A. M. Zhang, “Improved three-dimensional bubble dynamics model based on boundary element method,” Journal of Computational Physics, 294, 208-223, (2015)

[12] S. P. Wnag, Y. L. Liu, Q. X. Wang, A. M. Zhang, “The motion of a 3D toroidal bubble and its interaction with a free surface near an inclined boundary,” Physics of Fluids, 28, 122101, (2016)

[13] J. H. Duncan, S. Zhang, “On the interaction of a collapsing cavity and a compliant wall,” Journal of Fluid Mechanics, 226, 401-423, (1991)

[14] K. M. Kalumuck, R. Duaiswami, G. L. Chahine, “Bubble dynamics fluid-structure interaction simulation by coupling fluid BEM and structural FEM codes,” Journal of Fluids and Structures, 9, 861-883, (1995)

[15] J. H. Duncan, C. D. Milligan, S. Zhang, “On the interaction between a bubble and a submerged compliant structure,” Journal of Sound and Vibration, 197, 17-44, (1996)

[16] K. Tanizawa, “Nonlinear simulation of floating body motions in waves,” International Offshore and Polar Engineering Conference, Proceedings of the Sixth, (1996)

[17] C.H. Kim, A. H. Clement, K. Tanizawa, “Recent research and development of numerical wave tanks,” Journal of Offshore and Polar Engineering, 9, 4, (1999)

[18] Q. X. Wang, “Unstructured MEL modelling of nonlinear unsteady ship waves,” Journal of Computational Physics, 210, 368-385, (2005)

[19] Z. Li, L. Sun, Z. Zong, “Numerical analysis of gas bubbles in close proximity to a movable or deformable body,” Arch. Appl. Mech., 83, 1715-1737, (2013)

[20] C. T. Hsiao, A. Jayaprakash, A. Kapahi, L. Chahine, “Modeling of material pitting from cavitation bubble collapse,” Journal of Fluid Mechanics, 13, 1346, (2014)

[21] Z. Zong, J. X. Wang, L. Zhou, G. Y. Zhang, “Fully nonlinear 3D interaction of bubble dynamics and a submerged or floating structure,” Journal of Applied Ocean Research, 53, 236-249, (2015)

[22] S. Li, R. Han, A. M. Zhang, Q. X. Wang, “Analysis of pressure field generated by a collapsing bubble,” Ocean Engineering, 117, 22-38, (2016)

[23] S. Li, R. Han, A. M. Zhang, “Nonlinear interaction between a gas bubble and a suspended sphere,” Journal of Fluids and Structures, 65, 333-354, (2016)

[24] P. Cui, A. M. Zhang, S. P. Wang, “Small-charge underwater explosion bubble experiments under various boundary conditions,” Journal of Physics of Fluids, 28, 117103, (2016)

[25] A. M. Zhang, W. B. Wu, Y. L. Liu, Q. X. Wang, “Nonlinear interaction between underwater explosion bubble and structure based on fully coupled model,” Journal of Physics of Fluids, 29, 082111, (2017)